August 2018

A Molecular Dynamics Study of the Cellulose-Graphene Oxide Nanocomposites: The Interface Effects

Qian Mao
Clemson University, qianm@clemson.edu

A MOLECULAR DYNAMICS STUDY OF THE CELLULOSE-GRAPHENE OXIDE NANOCOMPOSITES: THE INTERFACE EFFECTS

A Dissertation
Presented to
the Graduate School of
Clemson University

In Partial Fulfillment
of the Requirements for the Degree
Doctor of Philosophy
Mechanical Engineering

---

by
Qian Mao
August 2018

Accepted by:
Dr. Huijuan Zhao, Committee Chair
Dr. Hongseok Choi
Dr. Gang Li
Dr. Srikanth Pilla

ABSTRACT

Cellulose has gained increasing attention due to its abundance and renewability. Obtained through a strong acid hydrolysis treatment of cellulose microfibrils, cellulose nanocrystals (CNCs) stand out among all hierarchical cellulose structures with appealing mechanical and optical properties that have been utilized as a reinforcing nanomaterial for the advanced material design. The cellulose nanocrystal graphene oxide (CNC-GO) nanocomposite film has been developed and successfully applied in portable and bendable sensing optoelectronics, energy storage and electromagnetic pulse protection devices. New material phenomena have been observed through experimental characterizations, but they lack fundamental understanding due to the experimental limitations in nanoscale. Therefore, a systematic and theoretical study at atomic level is desired to address the key factors responsible for the associated material properties of the CNC-GO nanocomposite, especially at its interface.

We adopt molecular dynamics (MD) simulation techniques to investigate the role of the hydrogen bonds in the CNC-GO interface interaction with respect to the CNC slab orientation, the CNC slab thickness, the GO oxidation type, and the water content at the interface. The objective is to understand the role of hydrogen bonds at the CNC-GO interface in CNC morphological variations and the mechanical property enhancement. We systematically investigate (1) the crystallography of the CNC-GO nanocomposites and their lattice parameter variations for the suppression of (200) facet in the X-ray diffraction (XRD) spectrum; (2) the hydrogen bond formation, types and distributions of the CNC due

to the CNC-GO interface interaction; and (3) the mechanical property variations due to the interface hydrogen bonding of the CNC-GO nanocomposites.

Through systematic molecular dynamics simulations of a set of simplified CNC-GO sandwich structures, the mechanism behind local (200) facet manipulation, as well as the global morphological variations, can be elucidated. It will shed light on the correlations between interface types and mechanical loading responses along with the interface water molecules for the mechanical performance enhancement. This research provides an understanding of intrinsically manipulating the CNC-GO interface and potentially engineering the cellulose based nanocomposite materials and mechanical properties for future advanced materials development.

DEDICATION

I dedicate this dissertation to my family for their love and support.

ACKNOWLEDGMENTS

The completion of this undertaking could not have been possible without the participation and assistance of so many people. Their contributions are sincerely appreciated and acknowledged.

I would like to express my sincere gratitude to my advisor, Professor Huijuan Zhao, for her endless patience, excellent suggestions and constructive guidance. Her constant support and encouragement are deeply appreciated. I would like to thank my committee members, Professor Hongseok Choi, Professor Gang Li, and Professor Srikanth Pilla for their constructive review of this work and valuable suggestions.

I wish to express my thanks to the undergraduate laboratory coordinator Dr. Todd Schweisinger and my colleagues during the time we had been working as lab TAs for three and a half years. Their precious suggestions, kindness and encouragement help me construct my personality, communication skills, and leadership. I would like to thank our research collaborator, Professor Hongli Zhu, for her mentoring and encouragement. I would also like to thank my group members and my friends who have in one way or another shared their support, either intellectually, financially, mentally or physically during the past four years at Clemson: Dr. Chengjian Li, Dr. Yingye Gan, Li Shi, Sandeep Rao, Weifeng Wu, Vishnupriya Ramineni, Zibusiso Dhlamini, Sarah Collings, Baobao Tang, Dr. Qi Liu, Dr. Hua Li, Dr. Jian Zhou, Dr. Jingyuan Yan, Dr. Qing Mao, Longsheng Jiang, Sheng Fu, Xiao Jia, Yuxin Li, Junkui Huang, Zhengshou Lai, Mitra Shabani, etc.

I am deeply indebted to my parents and my parents in law, whose value to me only grows with age. Finally, I acknowledge my husband, Chao Tang, for his countless support and love.

TABLE OF CONTENTS

LIST OF TABLES

LIST OF FIGURES

I. INTRODUCTION

1.1 Background and Motivation

Native cellulose, the major component of cell walls from vascular plants, has two distinct crystal structure forms: Iα form, which is a single-chain triclinic phase; and Iβ form, which is a two-chain monoclinic phase [1][2][3]. Through the first principles theory calculation, Iβ cellulose is found to have better stability compared to the Iα cellulose due to the rotation in the Iβ origin chain plane relative to (200) plane and the electrostatic interaction in the Iβ center chain plane [4][5]. The Iβ cellulose nanocrystals (CNCs) extracted by submitting cellulose microfibrils to a strong acid hydrolysis treatment, possess numerous appealing properties such as large surface area, low density, good toughness and strength. In addition, they have strong resistance to moisture, sunlight, usual pollutants or even acid attack at the moderate temperature. Meanwhile, they can be easily chemically modified and are biodegradable [6][7]. Therefore, Iβ CNCs have been widely used as the fundamental reinforcing matrix embedded with graphene or graphene oxide (GO) for smart CNC based nanocomposite membranes. Graphene and GO are 2-dimensional (2D) materials that contain a single layer of carbon atoms arranged in a hexagonal lattice. Unlike graphene, GO oxidized by strong oxidizers entails thousands of super hydrophilic functional groups, which introduces more extensive fiber matrix interaction in the nanocomposites [8]. The most widely accepted GO structure proposed by A. Lerf and J. Klinowski [9] indicates the presence of carboxyl groups (-COOH) on the periphery of the

basal plane of GO as well as hydroxyl groups (-OH) and epoxy bridges (-C-O-C-) in the center through nuclear magnetic resonance (NMR) spectroscopy [10]. However, the particular structures and properties of GO highly depend on the synthesis method and the degree of oxidation.

Iβ CNC and GO have attracted great attention as the matrix and reinforcement materials for the cellulose nanocomposites development [11][12]. R. Xiong *et al.* [13] observed that at the GO:CNC ratio about 1.6:1, the tensile strength of the membrane increased to 490±30 MPa and toughness to 3.9±0.5 MJ/m^3, exhibiting better performance than pristine membranes. Y. Wen *et al.* [14] fabricated ultra-strong CNC-GO membranes via evaporation-induced assembly with the CNC ranging between 2.5 wt.% and 10 wt.%. The tensile strength was enhanced up to 765±43 MPa and the toughness to 15.64±2.20 MJ/m^3, which were 1.79 and 2.06 times than those of pristine membranes prepared through the same procedures. The significant enhancement in the material properties of CNC based nanocomposite membranes is attributed to the good dispersion of the reinforcement elements graphene and GO, giving the chance to the chemical and physical bond formations, especially the strong hydrogen bonding networks at the matrix-reinforcement interface [15]. And in some cases of being immersed into the explicit aqueous solvent, the cellulose face is able to either form a stable complex with a reinforcement of graphene, or exhibit conformational rearrangement with disturbed intra and inter hydrogen bonding [16]. There also have been numerous studies on the different binding sites of CNC or GO as CNC-GO nanocomposite membranes were fabricated through different approaches. K. K. Sadasivuni *et al.* [12] modified the CNC-GO nanocomposite membranes with isophorone

diisocyanate involved in m-(CNC-GO) synthesis reaction, and the eco-friendly proximity sensors that detect physical touch and pressure sensing were made with faster response and higher sensitivity. S. Montes *et al.* [17] produced the cellulose nanocrystal-stabilized graphene poly (vinyl alcohol) (GR-CNC/PVA) nanocomposite membranes by the casting method, and GR-CNC/PVA exhibited superior mechanical properties than pristine PVA, CNC/PVA or GR/PVA, attributed to the strong hydrogen bonding between PVA and GR-CNC. R. Kabiri *et al.* [18] synthesized highly flexible nanocomposite membranes of nanocrystalline cellulose acetate (NCCA) and graphene oxide (GO) also by the casting method, and the NCCA-GO membranes demonstrated mechanical property enhancement relative to NCCA matrix and improved barrier properties against water vapor.

Meanwhile, cellulose nanocomposites can be designed to have high conductivity [19][20], remarkable cycle stability, and high specific capacitance [21]. Therefore, cellulose nanocomposites products have promising applications in portable and bendable paper electronics, energy storage devices, and electromagnetic pulse protection devices [22][23]. And it is of the great significance to understand the matrix-reinforcement interface interaction of cellulose nanocomposites and the correlation with the various properties at a fundamental level, which can potentially broaden the knowledge of cellulose nanocomposite behaviors, provide a helpful guidance for the future industrial applications, as well as facilitate the cellulose nanocomposites development.

1.2 Structure Descriptions

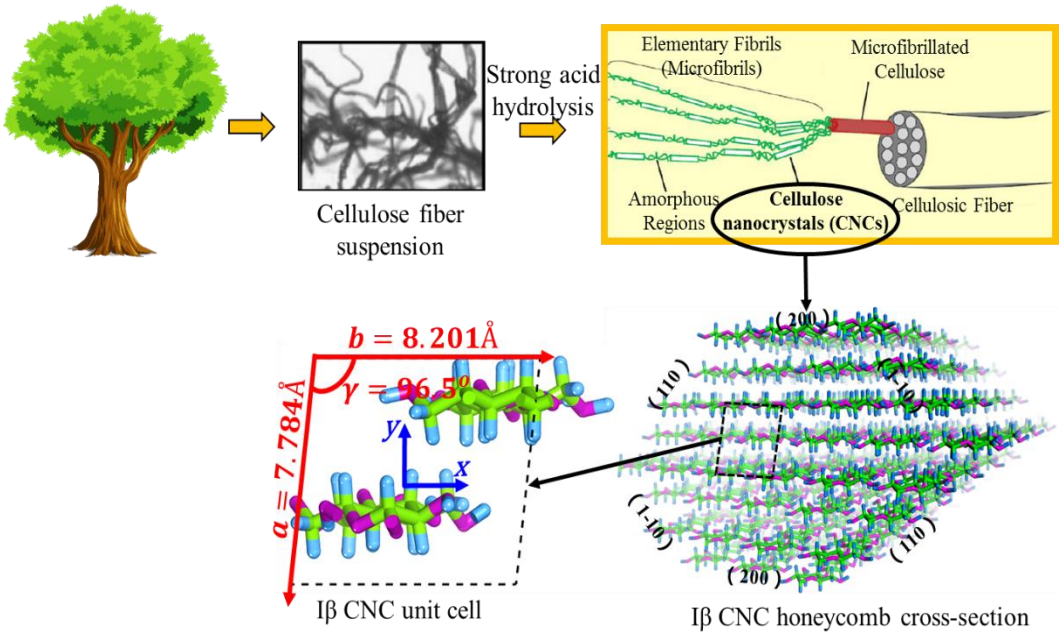

Figure 1. 1: From the cellulose sources to Iβ CNC unit cell atomic structure. The Iβ CNC cross-section is honeycomb shape with planes (110) and (1-10) that show the hydrophilic character, and plane (200) that shows the hydrophobic character (bottom right); the Iβ CNC unit cell (bottom left) contains a center chain on top and an origin chain on bottom of the unit cell, where the green, cyan and magenta atoms represent carbon, hydrogen and oxygen atoms, respectively, and the lattice parameters are a =7.784 Å, b =8.201 Å, c =10.380 Å, $\alpha = \beta$ =90° and γ =96.5° [29].

As shown in Figure 1. 1, Iβ CNCs are cellulose structures in suspension grown under strong acid hydrolysis with strictly controlled conditions (controlled temperature, agitation, and time), leading to the decomposition of the amorphous regions and the formation of high-purity single crystals. The resulting suspension is then washed by successive centrifugations followed by dialysis using distilled water to remove any free acid molecules [24][25]. The cross-section of the Iβ CNC elementary fibril is commonly interpreted to contain planes (110) and (1-10) that show the hydrophilic character, and plane (200) that shows the hydrophobic character [26][27][28]. The $P2_1$ space group of Iβ

CNC and its unit cell parameters (see the caption of Figure 1. 1) have been determined via X-ray structure refinement (SHELX-97) by Y. Nishiyama *et al.* [29], and they also have confirmed the hydroxymethyl group conformations of two chains within the unit cell to be both in "*tg*" (trans and gauche+). In one Iβ CNC unit, three -OH groups are available for the strong dipole-dipole interaction (hydrogen bonds) and the weak *van der Waals* interaction [7]. In the presence of a great amount of -OH and -COOH functional groups on the GO surface, hydrogen bonds are formed at the interface of Iβ CNC-GO, which substantially affect the CNC lattice parameters and the CNC-GO supercell, CNC's morphological characterizations such as axial tilt of the molecular chains, dihedral angle variations of hydroxymethyl groups, flip motion of the terminal groups etc., as well as the chemical, electrical, mechanical and thermal properties of the CNC-GO nanocomposites [13][30].

1.3 State of the Art and Research Objectives

Many experimental techniques have been utilized to analyze the hydrogen bonding networks. The synchrotron X-ray and the neutron diffraction along with the Fourier-difference analysis are used to determine the positions of carbon/oxygen atoms as well as hydrogen atoms [29]. Polarized spectra of FTIR data is adopted to obtain weakening and ruptures of hydrogen bonds upon heating based on partially disordered systems [31]. The X-ray powder diffraction (XRD) has identified the peak suppression at the CNC-GO interface [8], but the interpretation of the morphological variations at the CNC-GO interface as well as the determination of the associated hydrogen bonding mechanisms for

the property enhancement are unclear. Therefore, systematically investigating the mechanisms behind all these aspects through the numerical simulation is of high priority.

Molecular Dynamics (MD) simulations have been widely employed to investigate the mechanical properties [32], thermal properties and interface interaction of Iβ CNC [33]. The reactive force field (ReaxFF) [34] has been tested to be the most versatile and accurate reactive potential to predict the chemical, mechanical and thermal properties of Iβ CNC [35]. Meanwhile, ReaxFF force field is capable to capture the bond forming and breaking for the covalent bonds, and detail the non-bonded interactions, especially giving the explicit description for hydrogen bonds [33][35][36]. MD investigations with the use of ReaxFF force field have been done in the mechanical property evaluations on the pristine CNC, wet GO, and simple CNC-GO composite models without concerning the presence of water molecules at the interface and structural variables that may have significant effects on the determination of the mechanical properties [30][35][37][38].

In this research, we adopt the ReaxFF force field in the MD large-scale atomic/molecular massively parallel simulator (LAMMPS) [39] to systematically investigate the CNC-GO interface interaction based on Iβ CNC-GO sandwich structures with respect to various CNC slab thicknesses, surface orientations, GO oxidation types, and water contents at the CNC-GO interface. The objective of this research is to understand the role of hydrogen bonds in altering CNC-GO lattice parameters as well as the CNC morphologies in the presence of the CNC-GO interface, and then provide a rationale correlated with the hydrogen bonding mechanisms for the mechanical property enhancement of the CNC-GO nanocomposites.

II. INTRODUCTION TO MOLECULAR DYNAMICS SIMULATION

2.1 The Basic Molecular Dynamics Algorithm

In MD simulation, the classical mechanics is adopted to accurately predict the motion of any particle-like objects by solving Newton's Second Law, $\boldsymbol{F}=m\boldsymbol{a}$, where $\boldsymbol{F}$ is the force vector, m is the atomic mass, and $\boldsymbol{a}$ is acceleration vector [40]. The MD simulation can provide detailed trajectory information of atoms and molecules in materials [41]. The simplified algorithm of how MD proceeds is illustrated in Figure 2. 1.

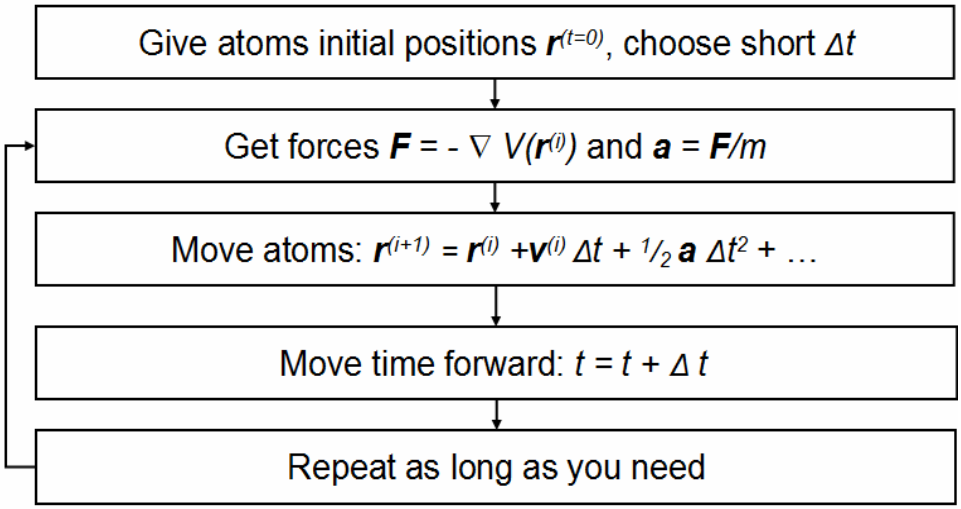

Figure 2. 1: A simplified description of the standard MD simulation algorithm. In practice, MD codes use more complicated versions of this algorithm that incorporate temperature and pressure controls.

Giving the initial positions and velocities for each atom and applying the interatomic potential for the entire system, the forces of each atom can be derived through the first order derivative of the potential with respect to the atom coordinates, and the acceleration can be then calculated using Newton's Second Law. Through the time integration with respect to the timestep Δt, the atom positions and velocities will be updated. Such procedure can be repeated as long as necessary until reaching to the desired material

condition. In MD simulation, the proper timestep size is in femtoseconds. A typical MD simulation requires over a million timesteps until the system reaches to the desired condition.

In the courses of a simulation, parameter outputs at each timestep can be pulled out, including system dimensions, atom velocities, forces, momenta, energy components, etc. Properties that can be calculated through original outputs or statistical postprocessing are:

(1) Structural and mechanical properties;

(2) Thermal expansion coefficient, glass transition temperature and melting point;

(3) Grain boundary structure, defect structure, diffusion and sliding;

(4) Thermal conductivity, heat capacity, free energy difference between phases;

(5) Radial distribution function, X-ray diffraction, diffusion coefficient for liquids;

(6) Fast plastic flow, crack growth and fracture propagation, shock wave propagation, irradiation, cluster impact, operation of nanogear.

MD is advantageous over density functional theory (DFT) since it is extremely fast and it is able to process millions of atoms in one system. However, some of the drawbacks of MD include:

(1) The potential is system independent, and the accuracy of a potential is continuously under question.

(2) The length scale and time scale are limited, not a desired fit for the macroscopic simulations.

(3) Since there are no electrons including in the modeling, the electromagnetic properties are by no means available.

2.2 Ensembles

Although integrating Newton's equations of motion allows the constant-energy surface of a system, one may need to keep the temperature and pressure constant during the molecular simulation. LAMMPS provides several ensembles for controlling temperature, pressure and energy, depending on which state variables are kept fixed. For example, the energy E, the volume V, the temperature T, the pressure P, the enthalpy H, and the number of particles N. The number of particles in all ensembles is conserved, thus the available ensembles are: constant volume, constant energy (NVE); constant volume, constant temperature (NVT); constant pressure, constant temperature (NPT); constant pressure, constant enthalpy (NPH).

NVE ensemble, also known as the microcanonical ensemble, is obtained by solving Newton's equation without any temperature and pressure controls. Energy is conserved when this ensemble is generated. NVE ensemble is not recommended for equilibration, since the desired temperature cannot be achieved without energy flow facilitated by the temperature control methods. However, this is a useful ensemble if the constant-energy surface of the conformational space is a point of interest. NVT ensemble, also referred to as the canonical ensemble, is obtained by controlling the temperature through direct temperature scaling during the initialization stage and by temperature-bath coupling during the data collection stage. The volume is kept constant throughout the run. NVT ensemble is an appropriate choice when conformational searches of molecules are carried out in

vacuum without periodic boundary conditions [42]. NPT ensemble allows control over both the temperature and pressure. The unit cell vectors are subject to change, and the pressure is adjusted by changing the volume. This ensemble is typically used when the correct pressure, volume, and densities are important in the simulation. This ensemble can also be used during equilibration to achieve the desired temperature and pressure before changing to NVT or NVE ensemble when data collection starts [43]. NPH ensemble is the analogue of NVE ensemble. The enthalpy H (the sum of E and PV) is constant when the pressure is kept fixed without any temperature control. In NVT and NPT ensembles, the temperature must be controlled with an algorithm, which is called a thermostat. Note that the goal is not to keep the temperature constant, as that would mean fixing the total kinetic energy, which would be far off the aim of NVT and NPT. Rather, it is to ensure that the average temperature of a system is the desired one.

2.3 Thermostats

There are a number of thermostats that are commonly used, each of which has its advantages and disadvantages in terms of reliability, accuracy, and computational expense. The Langevin thermostat follows the Langevin equation of motion rather than Newton's, where a frictional force proportional to the velocity is added to the conservative force, which adjusts the kinetic energy of particles so that the temperature is correct [44]. The Anderson thermostat couples the system to a heat bath at the desired temperature. The bath is represented by collisions with a stochastic particle on randomly selected system particles. It has been found that the addition of stochastic collisions to the Newtonian MD system results in the simulation being a Markov chain that is irreducible and aperiodic, which

implies that the generated distribution with Anderson's algorithm is not a canonical distribution [45]. Nose-Hoover thermostat is not only for simulations in ensembles other than constant NVE, but also as a stable and efficient approach to perform simulation in which an expensive optimization has to be performed at each timestep. The Berendsen thermostat overcomes the main problem of a velocity-rescaling method that the temperature fluctuations are not allowed in the NVT ensemble [46].

2.4 Barostats

A constant pressure simulation can be conducted by using a "barostat" constructed with additional pressure-controlling variables [47][48]. These variables and their dynamics model the external environment and regulate the time-averaged values of temperature and pressure [49]. The common barostats are Nose-Hoover, Andersen and Berendsen. The Nose-Hoover barostat is the default barostat of the NPT ensemble implemented in LAMMPS. The Andersen barostat is an extended system method (comparing with the Nose-Hoover thermostat), which involves coupling the system to an external variable, the volume of the simulation box. It mimics the action of a fictional piston on a real system, with a user supplied mass, to control the volume of the simulation cell [50][51][52]. The Berendsen barostat is similar to the thermostat. The system is weakly coupled to an external bath using the principle of the least local perturbation. Similar to the temperature coupling, an extra term is added to the equations of motion that affect a pressure change [46].

2.5 Force Fields

A force field is a mathematical expression describing the dependence of the energy of a system on the coordinates of its particles. It consists of an analytical form of the

interatomic potential energy $U(\mathbf{r}_1, \mathbf{r}_2, ..., \mathbf{r}_N)$, and a set of parameters involved in this form [53]. The forces between the atoms or atom-like particles are described with interatomic potentials, or molecular mechanics "force fields". The force fields most commonly partition the N-body interactions into two parts: (1) bonded interactions: the summation of harmonic bonds, the associated angle and dihedral potentials (the latter is typically expressed by a periodic function such as a sinusoidal function); (2) non-bonded interactions: the pair force fields that contain long-range electrostatics and van der Waals interactions which incorporate repulsion and dispersion terms [54]. There are numerous force fields available in the literature with different degrees of complexity, and oriented to treat different kinds of systems. A typical expression for a force field is in the form of,

$$U = \sum_{bond} \frac{1}{2} k_b (r - r_0)^2 + \sum_{angle} \frac{1}{2} k_a (\theta - \theta_0)^2 + \sum_{torsion} \frac{V_n}{2} [1 + \cos(n\phi - \delta)] + \sum_{improper} V_{imp} + \sum_{LJ} 4\varepsilon_{ij} \left(\frac{\sigma_{ij}^{12}}{r_{ij}^{12}} - \frac{\sigma_{ij}^{6}}{r_{ij}^{6}} \right) + \sum_{elec} \frac{q_i q_j}{r_{ij}} \quad (2.1)$$

where k_b, k_a and V_n are force constants for bond-stretching, valence and dihedral angle deformation, respectively; r, θ and ϕ are the actual bond length, valence and dihedral angle values, respectively; r_0, θ_0 and δ are the optimal equilibrium bond length, valence and dihedral angle values, respectively; ε_{ij} and σ_{ij} are constants that describe the Lennard-Jones (L-J) term; q_i and q_j are charges of atoms *i* and *j*, and r_{ij} is their mutual distance. The first four terms present intramolecular or local contributions to the total energy (bond stretching, angle bending, and dihedral and improper torsions), and the last two terms

describe the repulsive and van der Waals interactions in 12-6 L-J form and the Coulombic interactions.

Force fields for specific systems are developed by fitting functions with parameters of experimental data via X-ray and electron diffraction, NMR, infrared, Raman and neutron spectroscopy, or with calculated data from ab initio or semi-empirical quantum mechanical calculations. The experimental data used for this process include equilibrium lattice parameter, cohesive energy, bulk modulus, elastic modulus, vacancy formation energies, thermal expansion coefficient, dielectric constants, vibration spectrum, and surface energy. Note that these empirical force fields are system specific. One should be careful about using one specific force field for other systems or conditions, since they oftentimes are not transferable. Even in the same system and conditions, some force fields may result in different dynamics since most of the potentials are usually constructed by fitting to static properties [40].

III. INTERFACE STRAIN IMPACT ON THE XRD PEAK SUPPRESSION OF THE CNC-GO NANOCOMPOSITES

3.1 Motivation

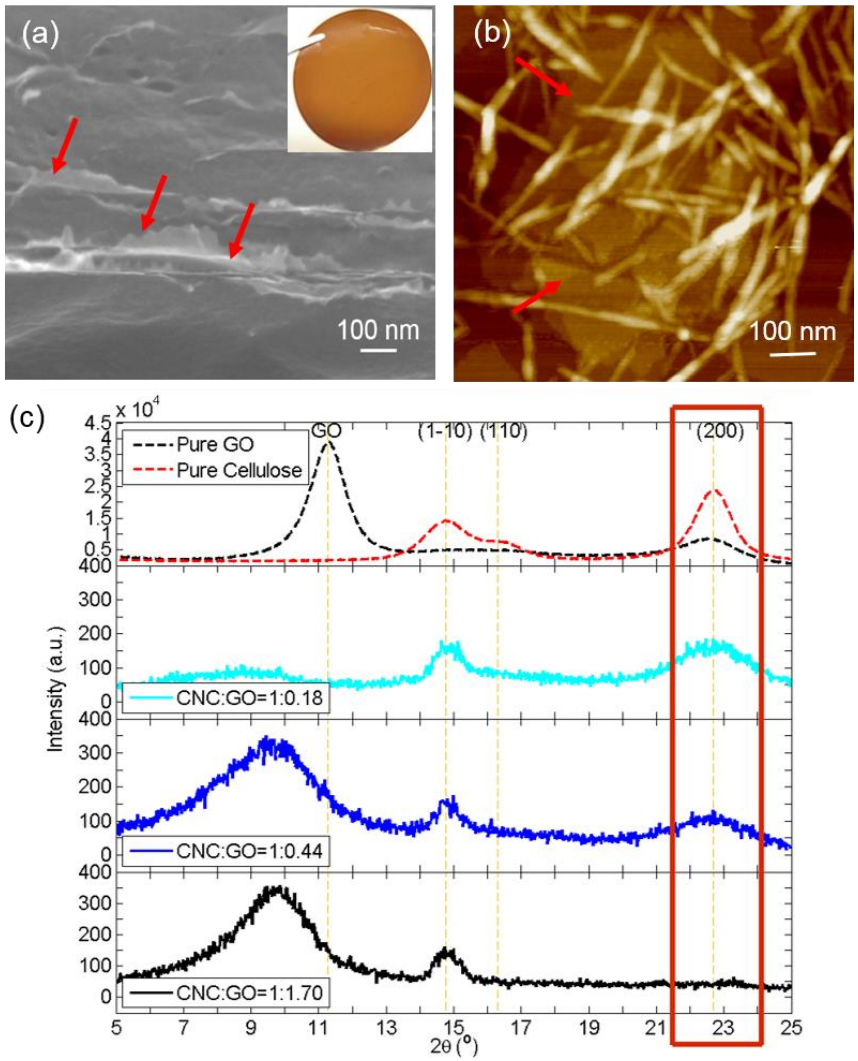

Figure 3. 1: The characterization of the CNC-GO nanocomposite film: (a) SEM image of the cross-section of the composite film with the red arrows indicating the monolayer of GO nanosheets, and the inset photograph shows the uniform CNC-GO hybrid film; (b) AFM image of the nanocomposite film surface with the randomly embedded CNC fibers and GO nanosheets, with the red arrows indicating the monolayer of GO nanosheets; (c) XRD spectrum of pristine GO (black dash line), pristine CNC (red dash line), and the composite films with various CNC:GO ratios.

In a nanocomposite, the fiber-fiber bonding and fiber-matrix adhesion are the dominant factors in determining the structures and properties of the material. The reinforcing effect of CNC is mainly due to the hydrogen bond formation among the CNC-CNC fibers and CNC-matrix. Various strategies have been adopted in order to achieve desired interface bonding at the CNC-matrix interface [55][56][57].

For the first time, Dr. Hongli Zhu's group from Northeastern University has found the suppression of the originally ordered CNC (200) facet with increasing concentrations of GO [8]. In that study, highly oxidized and single-to-few-layer GO was first mixed with the CNC in solution with different ratios for 72 hours and followed by vacuum filtration to form the nanocomposite film. As shown in the inset of Figure 3. 1 (a), the obtained film is smooth, flexible and uniform in thickness (~10 μm). Within the Scanning Electron Microscope (SEM) image of the nanocomposite film cross-section in Figure 3. 1 (a), a clear layer-by-layer structure can be observed, which contains two-dimensional (2D) monolayer GO nanosheets (as indicated by the red arrows in Figure 3. 1 (a)) and uniformly distributed CNC fibers in between. The surface morphology of the composite film at the nanoscale was observed with Atomic Force Microscopy (AFM) in Figure 3. 1 (b), from which the hybrid material contains CNC nanorods and monolayer GO nanosheets, indicated by the red arrows in Figure 3. 1 (b). XRD spectrum was performed to visualize the atomic and molecular structure of the crystalline domain in CNC, GO, and CNC/GO mixture with weight ratios from 1:0.18 to 1:1.70. As presented in Figure 3. 1 (c), the XRD diagram of the CNC shows three diffraction peaks at 2θ =14.7°, 15.9°, 22.7°, which are the characteristics of cellulose crystal assignments of the (1-10), (110), and (200) planes,

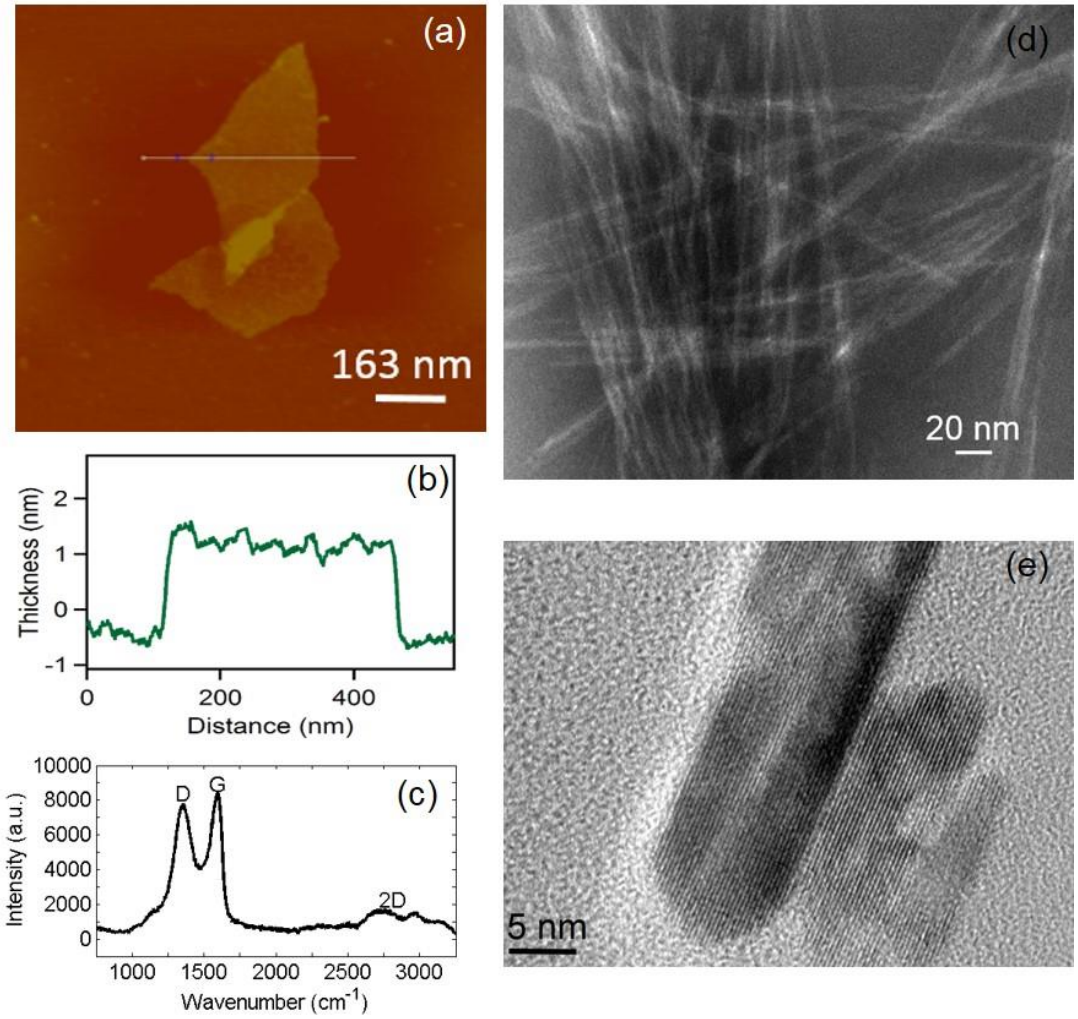

Figure 3. 2: Characterization of GO and CNC: (a) AFM image of GO; (b) the corresponding line scan of GO in (a); (c) Raman spectrum of pristine GO; (d)TEM image of CNC; and (e) HRTEM image of CNC.

respectively [58]. The crystallinity index (CrI) was calculated to be 89.70 % using the empirical Segal equation [59][60]. Interestingly, while the (110) facet remains, the (200) facet is weakened with the increase of GO:CNC ratio, which indicates that the originally ordered (200) facet (-CH-) arrangement is disrupted with the increasing GO concentrations. At the same time, the (200) peak of GO shifts from 2θ =11.3^o to 2θ =9.8^o due to larger layer spacing expanded by the interaction with cellulose [59].

Experimentally, morphology observation is the most direct method used to characterize the interaction between CNC nanorods and monolayers of GO nanosheets. A low concentration of highly oxidized GO was dropped onto a newly exfoliated surface of mica and then analyzed by AFM, as shown in Figure 3. 2 (a). The prepared GO nanosheets were dispersed in water very well with no aggregation. The planar size of the GO is ca. 150~200 nm, and the corresponding height profile is ca. 1.1 nm, indicating a complete exfoliation of GO to single-to-few-layer, shown in Figure 3. 2 (b). Through Raman spectroscopy, the GO was observed to show a D band at 1344 cm^{-1} and a G band at 1600 cm^{-1} respectively (Figure 3. 2 (c)). The intensity ratio, 0.92, of the D to G band (I_D/I_G) indicates a percentage of defects and disorder presented in the GO. Meanwhile, a significant feature and intensity of 2D bands is observed to locate between 2600~3000 cm^{-1} in the Raman spectrum, from which we can conclude that a certain percentage of synthesized GO is a monolayer. The morphology of the prepared CNC is characterized by Transmission Electron Microscope (TEM), shown in Figure 3. 2 (d). The average diameter of the CNC nanorods is approximately 3~10 nm with a length of approximately 100~200 nm. The High-Resolution TEM (HRTEM) image presented in Figure 3. 2 (e) well illustrates the ordered crystalline pattern in the CNC. As illustrated in Figure 3. 1 (b) the highly crystalline CNC nanorods were uniformly mixed with highly oxidized GO nanosheets to form hydrogen bonds, through which the two building blocks interact with each other at the interface to change the arrangements of the CNC chains.

Due to the limitation in the experimental characterization, there is an urgent need to fundamentally explain the suppression of the (200) peak of CNC of the nanocomposite.

In this study, we conduct the classical MD simulation to investigate the CNC-GO interaction with respect to the CNC slab thickness, the CNC surface orientation and the GO oxidation type. The objective is to gain the insight into the mechanism responsible for the (200) peak suppression in the CNC-GO nanocomposite.

3.2 Molecular Dynamics Setups

3.2.1 CNC-GO Sandwich Model

The number of cellulose molecule chains in Iβ CNC elementary fibrils and their cross-section shapes have long been under debate. One common observation contains a square cross-section with about 36 individual cellulose molecules of 3~5 nm in width and 50~500 nm in length [7][25][27]. Such a fibril structure only has two planes ((110) and (1-10) planes) exposed. Another observation has stated that the (200) plane can be exposed regardless of the cellulose chain number and the cross-section shape [58][61]. In order to systematically investigate the CNC-GO interface interaction, we adopt a sandwich structure with alternating monolayer GO and CNC slab with (200) and (110) orientations. For example, Figure 3. 3 (a) and (b) present the initial configurations of a 10-layer-CNC-slab with (200) face towards GO-COOH (denoted as CNC/10 (200) GO-COOH) and a 10-layer-CNC-slab with (110) face towards GO-OH (denoted as CNC/10 (110) GO-OH), respectively. The periodic boundary condition (PBC) is applied in three directions, which brings preexisting strain within the simulation domain without considering the actual shape and surface relaxation of CNC. However, such preexisting strain can be neglected and the clarity of CNC-GO interface morphological variations can be guaranteed. In order to investigate the hydrogen bond formation and their effects on the CNC-GO interface, we

adopt a GO layer with an experimentally achievable high oxidation ratio (44 %) [8]. The functional groups are set to be either -COOH or -OH. Figure 3. 3 (c) presents the three views of a monolayer graphene with randomly distributed -COOH functional groups. With Cellulose-Builder [62], the simulation box (supercell) is set to be 3.83 nm (width) × 5.17 nm (length) for CNC (200) GO cases, and 3.58 nm (width) × 5.19 nm (length) for CNC (110) GO cases. The CNC slab thicknesses vary among 8/7 layers ((200): 2.10 nm; (110):

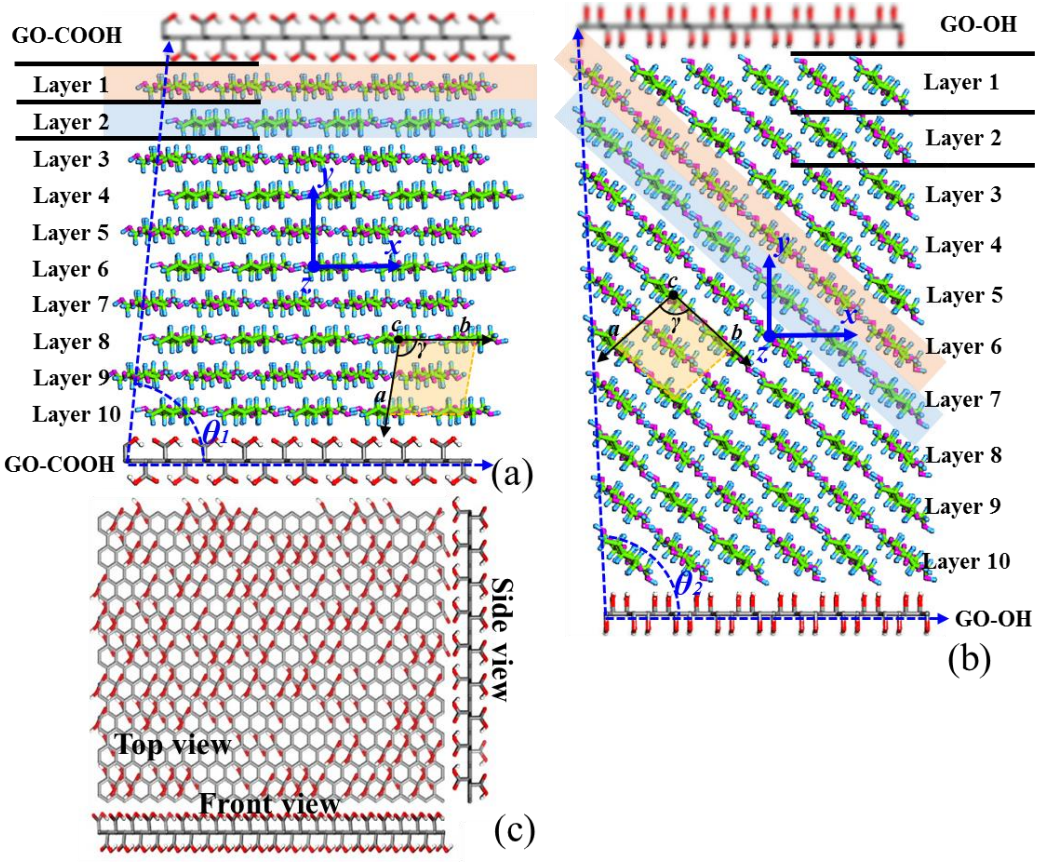

Figure 3. 3: Schematics of CNC-GO sandwich structures: (a) The CNC of 10-layer-slab with (200) face towards GO-COOH (denoted as CNC/10 (200) GO-COOH); (b) the CNC of 10-layer-slab with (110) face towards GO-OH (denoted as CNC/10 (110) GO-OH); (c) the monolayer graphene with randomly distributed -COOH functional groups (denoted as GO-COOH) from top, front and side views.

3.72 nm), 10 layers ((200): 3.87 nm; (110): 5.32 nm) and 20 layers ((200): 7.74 nm; (110): 10.64 nm) between two GO layers.

3.2.2 ReaxFF Force Field

Application of MD simulations to biomolecules is facilitated by several popular choices of force fields such as CHARMM27 [63], AMBER [64], COMPASS [65], Universal [66], Dreiding [67], cvff [68] and GROMOS [69]. The ReaxFF force field implemented in LAMMPS is more user-friendly, and it considers phenomena dependent not only on the reactivity of the involved species, but also on dynamic factors, such as diffusivity and solubility, affecting how species migrate through the system [70]. ReaxFF force field consists of fourteen terms and the associated tens of parameters obtained by first principles calculations. The general form of ReaxFF force field can be expressed in equation (3.1), where the bond energy E_{bond}, the atom under-coordination energy E_{under}, the valence angle energy E_{val}, the double-bond valence angle penalty E_{pen}, the torsion energy E_{tors}, and the conjugation energy E_{conj}, all involve the bond order function in equation (3.2). These potential terms are designed to respond dynamically to the local environment and to describe bond forming/breaking states [36]. Although they are roughly ten times slower than the use of the typical force fields expressed in equation (2.1), their extensive applications in hydrocarbons, nanotube systems, Si systems, and so on, have made this force field very popular and promising.

$$E_{system} = E_{bond} + E_{over} + E_{under} + E_{val} + E_{pen} + E_{tors} + E_{conj} + E_{vdWaals} + E_{Coulomb} \quad (3.1)$$

$$BO_{ij} = \exp[\, p_{bo,1} \cdot (\frac{r_{ij}}{r_{0,\sigma}})^{p_{bo,2}}\,] + \exp[\, p_{bo,3} \cdot (\frac{r_{ij}^{\pi}}{r_{0,\pi}})^{p_{bo,4}}\,] + \exp[\, p_{bo,5} \cdot (\frac{r_{ij}^{\pi\pi}}{r_{0,\pi\pi}})^{p_{bo,6}}\,] \qquad (3.2)$$

where r_0 are equilibrium bond lengths, $P_{bo,1}$ and $P_{bo,2}$, $P_{bo,3}$ and $P_{bo,4}$, $P_{bo,5}$ and $P_{bo,6}$ are the factors and exponential terms of σ, π and $\pi\pi$ bonds, respectively. This generates a differentiable potential energy surface, as required for the calculation of interatomic forces. This bond-order formula accommodates long-distance covalent interaction characteristics in transition state structures, allowing the force field to accurately predict reaction barriers [71].

X. Wu *et al.* [72] studied the elastic moduli and hardness of a cellulose Iβ crystal using uniform deformation and nanoscale indentation methods via ReaxFF force field. The elastic moduli in three lattice axes *a*, *b* and *c* were found to be 7.0±1.7 GPa, 28.8±2.9 GPa and 139.5±3.5 GPa, respectively, all of which were within the range of previous experimental and simulation results. The prediction transverse elastic modulus was E_T = 5.1±0.7 GPa which is in good agreement with atomic force microscopy nanoscale indentation results. Further analysis of the various energetic contributions, especially hydrogen bonding characterized in an explicit way in ReaxFF revealed different deformation mechanisms in three lattice directions [73]. F. L. Dri *et al.* [35] systematically evaluated three ReaxFF parameter sets (ReaxFF-Mattson [74], ReaxFF-Chenoweth [34], and ReaxFF-Rahaman [75]) with specifically selected hydrogen bond cutoffs and two

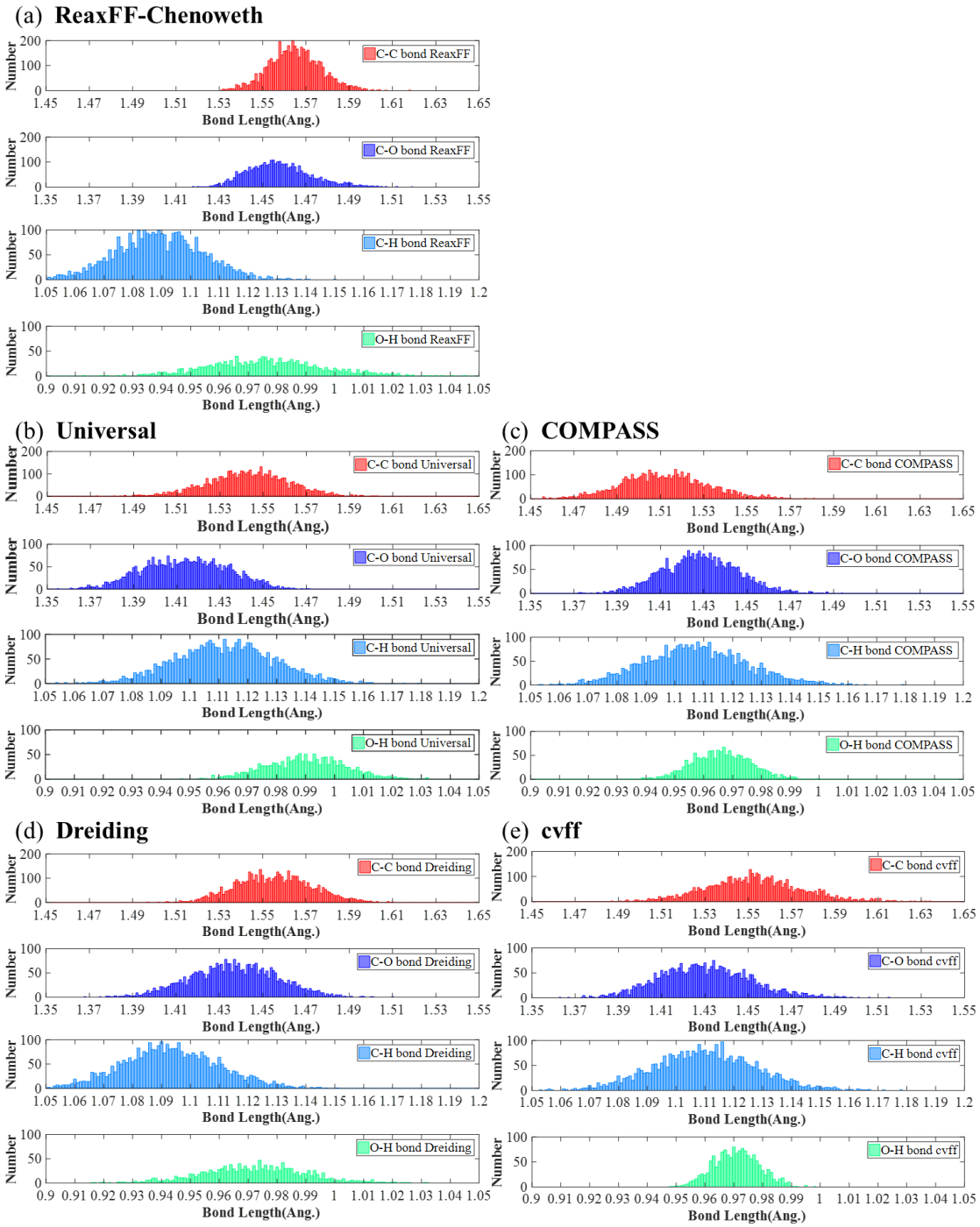

Figure 3. 4: The C-C, C-O, C-H and O-H bond length distributions for the pristine Iβ CNC structure with respect to different force fields at 100 K: (a) ReaxFF; (b) Universal; (c) COMPASS; (d) Dreiding; (e) cvff.

commonly-used non-reactive force fields (COMPASS and GLYCAM [76]) in terms of

their capability of predicting lattice parameters, elastic constants, coefficients of thermal expansion, the anisotropy of Iβ cellulose, etc. The best prediction in lattice constants was obtained by using ReaxFF-Chenoweth (the one used in our current research). All force fields studied could predict the elastic moduli within the range, except COMPASS for E_{22}, and ReaxFF-Chenoweth yielded the best result for transverse moduli. And they concluded that ReaxFF-Chenoweth with a proper hydrogen bond parameter set was identified to provide most accurate predictions over other force fields. A. Paajanen *et al.* [77] investigated the thermal decomposition of the cellulose molecules and predicted the kinetics of the primary decomposition reactions with all hydrogen bond parameters carefully examined before ReaxFF simulation. The results suggested that, in gas-phase conditions at 1400 to 2200 K, the decomposition occurred primarily through random cleavage of the β (1→4)-glycosidic bonds, for which an activation energy of (171±2) kJ/mol. and a frequency factor of (1.04±0.12)×10^{15} s^{-1} were obtained. And the results indicated the support for further use of ReaxFF-based molecular dynamics simulations in cellulose pyrolysis.

We have tested the C-C, C-O, C-H, O-H bond length variations on the Iβ CNC structure with respect to various force fields for carbohydrates, i.e., ReaxFF-Chenoweth, Universal, COMPASS, Dreiding, and cvff, shown in Figure 3. 4. For the force field of ReaxFF-Chenoweth, shown in Figure 3. 4 (a), the concentrations of C-C, C-O, C-H and O-H bond lengths are within the ranges of experimental results [29][78]. As for the other force fields, Universal, COMPASS and cvff show significant errors in the C-H bond length distributions. The mean value of C-H bond length is measured to be 1.09 Å [79][80], but

the mean values of C-H bond length with the use of Universal, COMPASS and cvff are between 1.11 Å and 1.12 Å, yet showing extremely low intensity around 1.09 Å. Similar study has been conducted on the angle distributions. Except for ReaxFF-Chenoweth, none of the above force fields is good enough for C-C-C, C-O-C, C-C-O angle distributions. Therefore, we adopt the ReaxFF-Chenoweth in this study.

3.2.3 Simulation Setups

In this study, the selected CNC-GO sandwich structure reaches to the equilibrium condition under NPT ensemble with timestep 0.5 fs. Periodic boundary condition is considered in all three directions. The temperature is set to be 100 K. The room temperature is also tested, yet the results regarding the motions of -CH and -OH terminal groups and hydrogen bond formation are qualitatively the same as those at the temperature of 100 K. To carry out a better statistical analysis of the interface interaction without the complicated morphologies over elevated temperature, we select the temperature to be 100 K [73]. The room temperature 300 K is also tested and it shows that the hydrogen bonding networks are qualitatively the same as those at the temperature of 100 K but local high temperature conformations appear [72][77][81].

During the equilibration stage, Berendsen thermostat and Nose-Hoover barostat are adopted to control temperature and pressure, respectively. There are two methods we can utilize in LAMMPS for the pressure control: one is the isotropic pressure control, the other is the anisotropic pressure control. For the isotropic pressure control, the hydrostatic pressure is maintained at a desired value (0 atm. Gauge pressure in this study). However, the pressure components in each Cartesian direction are not necessary to be the desired

values. For the anisotropic pressure control, the pressure components P_{xx}, P_{yy} and P_{zz} are controlled independently. In other words, the isotropic pressure control will bring a preexisting stress field into the simulated systems if the material system is highly anisotropic. A typical computational model only considers Iβ cellulose as a single crystal excluding multiple orientations as well as surface and interface effects, thus the results predicted by anisotropic pressure control may be different from those via experiment.

3.3 Results and Discussion

The objective of the MD simulation is to adopt the simplified CNC-GO sandwich structure to understand the hydrogen bonding effects on the variations of (200) and (110) peak locations and intensities in the XRD spectrum with respect to the CNC slab orientation, CNC slab thickness and GO oxidation type.

3.3.1 Effects of Isotropic/Anisotropic Pressure Control

Figure 3. 5 shows the pressure component variations for the pristine CNC structure with respect to the CNC facet orientation and the pressure control setup. In Figure 3. 5, the black dash lines and the corresponding averaged magnitude of pressure components are calculated over a selected time interval [1,000 ps 1,600 ps] after the system reaches to the equilibrium. The amplitude of P_{yy} vibration is relatively smaller than the other two due to the pressure acting on the out-of-plane direction. With the relaxed CNC lattice, the average values of pressure components under anisotropic pressure control are all zeroes, regardless of the cellulose facet orientation. As for the isotropic pressure control, the mean values of pressure components P_{xx}, P_{yy} and P_{zz} are -0.47 GPa (tension), -0.32 GPa (tension) and

0.79 GPa (compression) for (200) orientation, and -0.24 GPa (tension), -0.55 GPa (tension) and 0.79 GPa (compression) for (110) orientation, respectively.

Table 3. 1 gives the box length variations of the pristine CNC supercells as shown in Figure 3. 3 (a) and (b) (the portion in the middle between two monolayer GOs) due to the isotropic and anisotropic pressure controls. Figure 3. 6 pictures the center of mass of each relaxed cellulose monomer under the isotropic and anisotropic pressure control

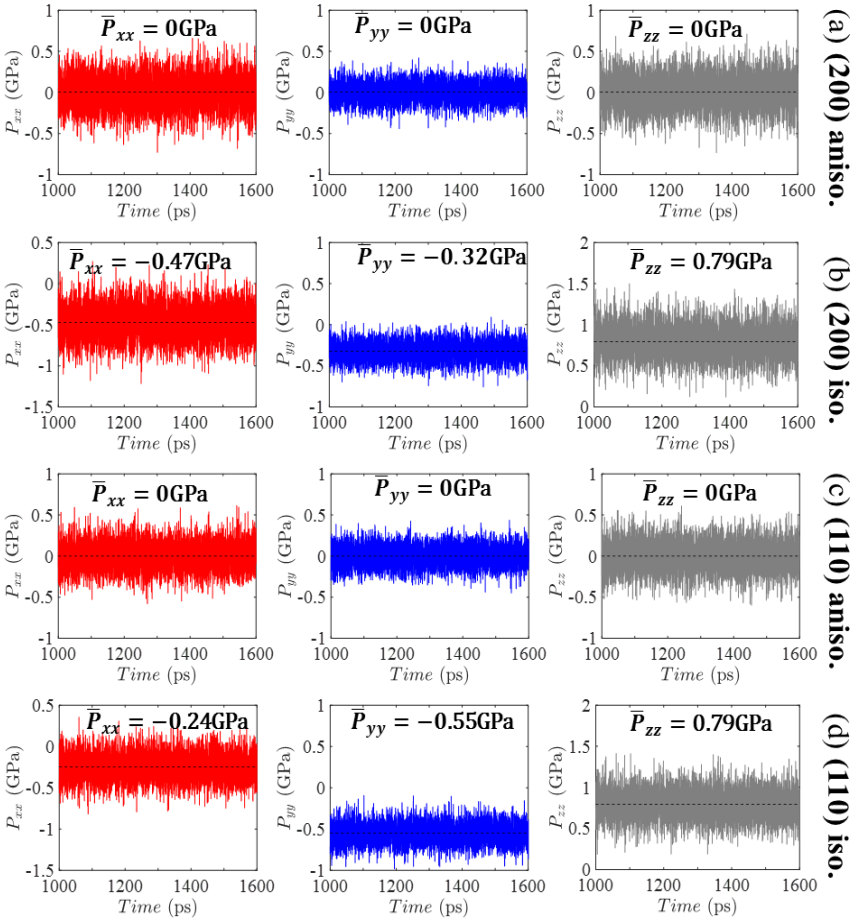

Figure 3. 5: Pressure components P_{xx}, P_{yy} and P_{zz} for pristine CNC bulk: (a) (200) orientation under anisotropic pressure control; (b) (200) orientation under isotropic pressure control; (c) (110) orientation under anisotropic pressure control; (d) (110) orientation under isotropic pressure control. The red, blue and grey plots represent pressure components in x, y and z directions, respectively.

conditions. It is obvious that there is huge shrinkage in l_x for (200) orientation and in l_y for (110) orientation under anisotropic pressure control.

	(200) Orientation				(110) Orientation			
	l_x (Å)	l_y (Å)	l_z (Å)	θ(°)	l_x (Å)	l_y (Å)	l_z (Å)	θ(°)
iso.	41.258 ±0.014	38.909 ±0.013	52.220 ±0.017	83.500	36.003 ±0.011	53.490 ±0.016	52.213 ±0.016	93.008
aniso.	38.580 ±0.019	39.603 ±0.022	53.318 ±0.017	83.500	36.193 ±0.015	49.798 ±0.020	53.214 ±0.015	93.008

Table 3. 1: The box length variations of the pristine CNC supercells as shown in Figure 3. 3 (a) and (b) due to the isotropic and anisotropic pressure controls. l_x, l_y and l_z represent the lengths in three orthogonal directions, and θ represents the angle between horizontal and tilted axes, labeled as θ_1 and θ_2 for (200) and (110) pristine CNCs in Figure 3. 3 (a) and (b), respectively. The lattice constants for three principal axes are l_x, $l_y / \sin\theta$ and l_z due to the monoclinic structure of the Iβ CNC.

Derived from the averaged centers of masses of each monomer (every two consecutive glucose rings) within the pristine CNC bulk, the lattice parameters of pristine

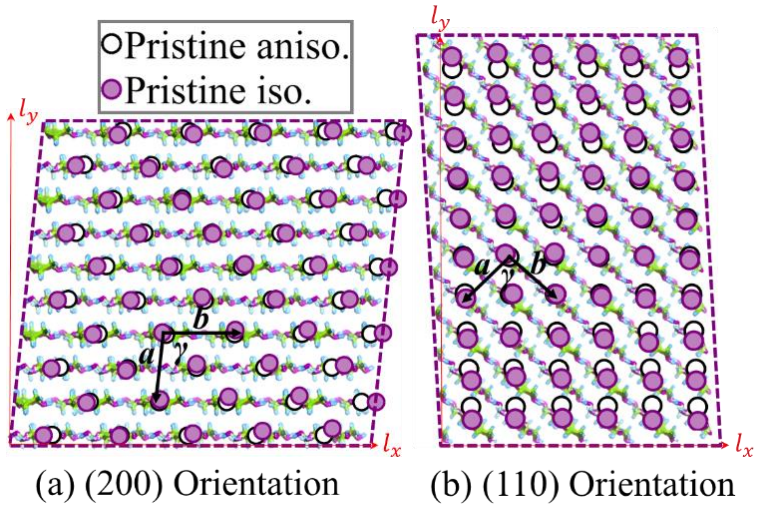

Figure 3. 6: The difference of supercell lattice variations between isotropic and anisotropic pressure controls. (a) Pristine CNC of (200) orientation; (b) pristine CNC of (110) orientation. The black open circles and purple solid circles represent the centers of masses of each cellulose monomer. The purple dash parallelogram represents the relaxed configuration of pristine Iβ CNC under isotropic pressure control with PBC imposed.

	a (Å)	*b* (Å)	*c* (Å)	*α* (°)	*β* (°)	*γ* (°)
Reference [29]	7.78	8.20	10.38	90.00	90.00	96.50
CNC (200) iso.	7.66 ±0.18	8.07 ±0.24	10.23 ±0.06	89.60 ±3.05	89.82 ±4.46	96.43 ±2.64
CNC (200) aniso.	7.78 ±0.07	7.53 ±0.07	10.41 ±0.04	90.00 ±0.73	90.00 ±0.79	96.50 ±0.88
CNC (110) iso.	7.65 ±0.22	8.09 ±0.27	10.22 ±0.07	89.94 ±3.25	89.93 ±4.61	96.40 ±2.79
CNC (110) aniso.	7.44 ±0.08	7.83 ±0.08	10.39 ±0.04	90.00 ±0.71	89.99 ±0.77	100.85 ±0.88

Table 3. 2: Lattice parameter variations for pristine CNC bulks of (200) and (110) orientations under isotropic and anisotropic pressure controls.

CNCs of (200) and (110) orientations under isotropic and anisotropic pressure controls are presented in Table 3. 2. With isotropic pressure control, the relaxed lattice parameters match well with the reference data, regardless of the orientation of the CNC structure. However, with anisotropic pressure control, the relaxed lattice parameters strongly depend on the CNC orientation. Compared with the reference data, CNC of (200) orientation shown in Figure 3. 3 (a) presents 8 % reduction in lattice constant *b*, CNC of (110) orientation shown in Figure 3. 3 (b) shows significant lattice parameter variations, not only with lattice constants *a* and *b*, but also with the lattice angle *γ*.

Since CNC is a highly anisotropic material in nature, the isotropic pressure control will cause a strong preexisting stress field within the CNC structure under PBC. However, the lattice constants predicted from isotropic pressure control are in alignment with reference experimental results. The possible reasons behind it are as follows: (1) The CNC fiber follows a hexagonal cross-section as shown in Figure 1. 1, which has three surface orientations (200), (110), and (1-10). Because of such surface confinement, the fully

relaxed CNC fiber might contain a preexisting stress field. (2) The PBC we adopt in this study brings a strong anisotropic effect to the material structure. With anisotropic pressure control, the CNC structure can be fully relaxed, which is contradictory to the real case. Therefore, the lattice parameters under anisotropic pressure control deviate from the reference results. In the following discussion, we will use these two pressure control methods and investigate the XRD spectrum variations of the CNC-GO sandwich structure with respect to the CNC slab thickness, the CNC slab orientation and the GO oxidation type.

3.3.2 XRD Spectra

The XRD spectra of GO interacting with CNC (200) and (110) facet slabs from MD simulations are plotted in Figure 3. 7 (a) and (b), respectively. The black and grey plots signify the pristine CNC bulks under isotropic and anisotropic pressure controls, respectively. The solid and dotted plots represent the sandwich structures under anisotropic and isotropic pressure controls, respectively. For CNC (200) with slab thicknesses to be 8, 10 and 20 layers, the CNC:GO molecular weight ratios are 1:0.1027, 1:0.2053, 1:0.2567 for the CNC (200) GO-COOH, and 1:0.0913, 1:0.1825, 1:0.2281 for the CNC (200) GO-OH, respectively. For CNC (110) with slab thicknesses to be 7, 10 and 20 layers, the CNC:GO molecular weight ratios are 1:0.0762, 1:0.1524, 1:0.2177 for the CNC (110) GO-COOH, and 1:0.0677, 1:0.1354, 1:0.1934 for the CNC (110) GO-OH, respectively.

For the pristine CNC bulk under isotropic pressure control, the characteristic peaks of (1-10), (110) and (200) planes are in good agreement with the reference values (shown as yellow dash lines on the background in Figure 3. 7) regardless of the orientation. The

(200) peak of (200) and (110) CNC bulks under anisotropic pressure control turn to shift leftward and rightward respectively, compared to those under isotropic pressure control. Nevertheless, the (110) peak of both (200) and (110) CNC bulks under anisotropic pressure

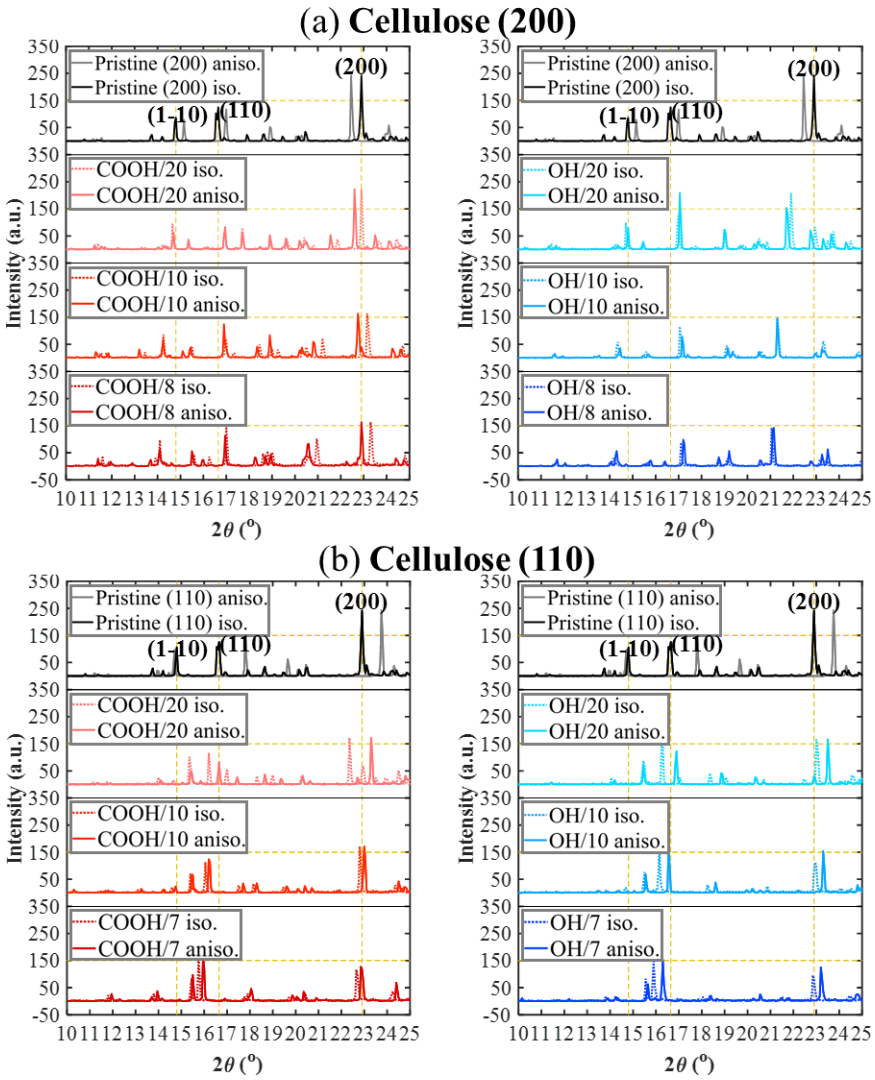

Figure 3. 7: Simulated XRD spectra with respect to various CNC slab orientations, thicknesses and GO oxidation types: (a) CNC slab of (200) orientation; (b) CNC slab of (110) orientation. For red and blue XRD plots, the solid lines represent the sandwich structures under anisotropic pressure control, and dotted lines represent the sandwich structures under isotropic pressure control. In (a) and (b), two GO oxidation types (-COOH and -OH on the left and right, respectively) and three CNC slab thicknesses are considered (20, 10 and 8 layers for CNC (200) cases; 20, 10, 7 layers for CNC (110) cases). The legend represents the GO oxidation type and the number of layers along CNC slab thickness direction, respectively.

control shift rightward, so does the (1-10) peak for (200) orientation under anisotropic pressure control. The (1-10) peak for (110) CNC bulk under anisotropic pressure control stays at about the same location as that under isotropic pressure control. In practice, the CNC membrane sample tested in experiment should include all possibilities of orientations. The fiber surface confinement limits the stress-free relaxation of the CNC fibers. The experimentally measured XRD spectrum has a relative wide peak, which reflects the superposition of the above considerations.

For the sandwich structures under anisotropic pressure control, as the CNC (200) facet interacts with GO, the CNC-GO interface distance is slightly different from the two CNC (200) layers' distance. Shown in red and blue solid lines of Figure 3. 7 (a), the (200) peak splits from 2θ =22.5º in the pristine CNC bulk to a range of 2θ =20.5º~23.5º in the sandwich structures with different intensity depending on the GO oxidation type. The split peak near 2θ =22.9º dominates when CNC (200) facet interacts with GO-COOH. The split peak near 2θ =21.0º~22.0º dominates when CNC (200) facet interacts with GO-OH. With the decreasing CNC slab thicknesses, the difference between (200) peaks of -COOH and -OH increases. On the other hand, the (1-10) peak and (110) peak slightly shift away from each other with no noticeable weakening with the decreasing CNC slab thicknesses, regardless of the GO oxidation type. In Figure 3. 7 (b), the interaction between the surface of the CNC (110) and GO cannot cause the significant weakening and shifting of the (200) peak in the corresponding XRD spectra. However, the (110) peak and (1-10) peak significantly shift towards each other with the decreasing CNC slab thicknesses, regardless of the GO oxidation type.

For the sandwich structures under isotropic pressure control, the (200) peak splits from 2θ =22.9º in the pristine CNC bulk to the identical range of 2θ =20.5º~23.5º as those under anisotropic pressure control, as shown in red and blue dotted lines of Figure 3. 7(a). The split peaks between 23.0º and 23.5 º have dominant intensities for the sandwich structures with GO-COOH interfaces, and the split peaks near 2θ =21.0º~22.0º have dominant intensities for the sandwich structures with GO-OH interfaces. As the CNC slab thickness decreases, the (200) peak of the GO-COOH sandwich structures gradually deviates from the anisotropic ones from left to right, whereas the (200) peak of the GO-OH sandwich structures firstly approaches to the anisotropic one from right to left, and then overlaps with it, and finally leaves it towards further left. In Figure 3. 7(b), similar to those under anisotropic pressure control, the interaction between the CNC (110) and GO cannot cause the significant weakening and shifting of the (200) peak. The (200) peaks of GO-COOH have slight shift from right to left, whereas the (200) peaks of GO-OH tend to stay around 23.0º as the CNC slab thickness decreases, whereas those under anisotropic pressure control exhibit more significant leftward shift. With the decrease of the CNC slab thickness, (1-10) and (110) peaks from both oxidation types shift towards each other. Meanwhile, the (110) peaks from both oxidation types have more leftward shift than those under anisotropic pressure control.

Figure 3. 7 shows that the splitting, weakening and shifting of the XRD peaks are greatly related with the CNC orientations, GO oxidation types and CNC slab thickness. These findings differ from the experimental observation shown in Figure 3. 1 (c) mainly due to the high crystallinity of the CNC slab and the simplicity of the single type CNC-GO

interface involved in the computational model. In spite of the discrepancies in XRD peak positions and intensities between two pressure controls, the common observations are that (200) peak tends to significantly shift and split as the thickness of CNC slab decreases in the (200) CNC-GO composite, whereas (1-10) and (110) peaks tend to shift towards each other as the thickness of CNC slab reduces in the (110) CNC-GO composite. In this way, we can gain the insight into the mechanism behind the (200) peak suppression as shown in Figure 3. 1 (c). To be more specific, we propose the following hypotheses: the (200) peak weakening observed in the experiments is mainly due to the interaction between the GO and the CNC (200) facets; the remaining (110) peak is mainly due to the interaction between the GO and the CNC (110) and (1-10) facets. The -COOH and -OH groups on GO both play different roles during the interaction with the CNC (200) facet. In the following discussion, further investigation on the conformation variations of CNC slabs are conducted to prove these hypotheses.

3.3.3 Discussion on lattice parameter variations

For any crystalline lattice, the location and intensity of the XRD peaks depend upon: (1) the size and shape of the unit cell, which determine the relative positions of the diffraction peaks; and (2) the atomic positions within the unit cell, which determine the relative intensities of the diffraction peaks [82]. Based on the MD simulation results, we can provide a fundamental understanding of the XRD peaks splitting, shifting and weakening observed in Figure 3. 7.

As we mentioned earlier, Iβ CNC structure belongs to the monoclinic crystal lattice. The *d*-spacing $d_{(hkl)}$ in XRD spectrum can be evaluated as

$$\frac{1}{d^2} = \frac{1}{\sin^2\gamma}\left[\frac{h^2}{a^2} + \frac{k^2}{b^2} + \frac{l^2\sin^2\gamma}{c^2} - \frac{2hk\cos\gamma}{ab}\right] \tag{3.3}$$

where d is the d-spacing, a, b, and γ are the lattice parameters, and h, k, and l are Miller indices to define the crystalline plane (hkl). The 2θ can be evaluated through the Bragg's Law: $n\lambda = 2d\sin\theta$, where λ is the wave length of the X-ray, and n is an integer. Therefore, the location of (1-10), (110) and (200) peaks are largely dependent on the magnitudes of a, b, and γ, since l equals 0. Although the increase in both a and b can cause a leftward shift of (110) and (1-10) peaks, the increase in a can cause a large leftward shift of (200) peak, whereas the variation of b cannot affect the location of (200) peak (k=0). An increase in γ

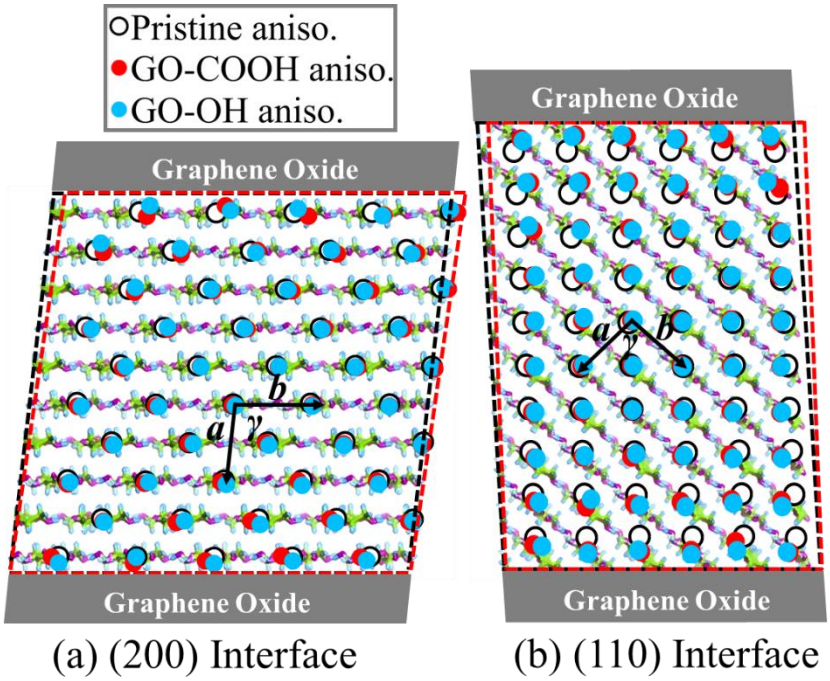

Figure 3. 8: Deformation due to the interaction at the CNC-GO interface under anisotropic pressure control. (a) 10-layer-CNC-slab with (200) facet interacted with GO; (b) 10-layer-CNC-slab with (110) facet interacted with GO. The circles and dots represent the centers of masses of each cellulose monomer (consecutive two glucose rings). The black and red dash parallelograms represent the relaxed configurations without the GO and with GO interactions containing -COOH functional groups, respectively.

causes a leftward shift of the (1-10) peak, a rightward shift of the (110) peak and a leftward shift of the (200) at a smaller magnitude.

Next, we will take the sandwich structures of 10-layer thickness as examples. For clarity, the structures discussed here only focus on anisotropic pressure control. The

	***a* (Å)**	***b* (Å)**	***γ* (°)**	***a* (Å)**	***b* (Å)**	***γ* (°)**
	CNC (200) + GO-COOH			**CNC (200) + GO-OH**		
20 layers aniso.	7.85±0.12	7.51±0.12	97.92±1.53	7.91±0.12	7.45±0.11	97.47±1.52
20 layers iso.	7.74±0.11	7.60±0.11	98.55±1.46	7.83±0.11	7.57±0.11	97.51±1.45
10 layers aniso.	7.88±0.17	7.54±0.17	99.31±2.15	7.93±0.17	7.47±0.15	98.39±2.13
10 layers iso.	7.73±0.16	7.61±0.17	99.93±2.05	7.92±0.17	7.55±0.17	97.75±2.32
8 layers aniso.	7.90±0.22	7.54±0.23	99.53±2.98	7.96±0.18	7.46±0.20	98.81±2.93
8 layers iso.	7.75±0.22	7.61±0.23	100.39±2.84	7.94±0.18	7.54±0.18	97.87±2.31
	CNC (110) + GO-COOH			**CNC (110) + GO-OH**		
20 layers aniso.	7.50±0.11	7.68±0.14	95.36±1.73	7.43±0.11	7.74±0.13	95.12±1.44
20 layers iso.	7.68±0.13	7.70±0.15	94.18±1.97	7.57±0.18	7.93±0.20	93.00±2.63
10 layers aniso.	7.56±0.14	7.64±0.18	94.80±1.97	7.51±0.19	7.73±0.22	93.92±2.96
10 layers iso.	7.67±0.19	7.68±0.22	94.40±2.89	7.60±0.29	7.95±0.39	92.39±6.90
7 layers aniso.	7.56±0.18	7.65±0.21	94.58±2.59	7.54±0.31	7.91±0.40	92.33±6.05
7 layers iso.	7.60±0.24	7.79±0.29	93.92±4.46	7.68±0.38	7.99±0.43	91.32±6.55

Table 3. 3: Lattice parameter variations with respect to the CNC face orientation, CNC thickness and GO oxidation type under anisotropic and isotropic pressure controls.

comparisons between isotropic and anisotropic pressure controls in terms of lattice parameters and (200) peak positions and intensities under both pressure controls will be

	CNC (200) + GO-COOH			CNC (200) + GO-OH		
	***2θ* (°) (MD)**	***2θ* (°) (Analytical)**	**Intensity (10^8) (Analytical)**	***2θ* (°) (MD)**	***2θ* (°) (Analytical)**	**Intensity (10^8) (Analytical)**
20 layers aniso./iso.	21.55/21.85	21.55/21.83	1.65/1.57	21.70/21.90	21.72/21.91	6.78/6.50
	22.60/22.90	22.59/22.88	8.70/8.95	22.70/21.95	22.77/22.96	3.38/3.84
10 layers aniso./iso.	20.80/21.20	20.82/21.21	0.66/0.54	21.30/21.30	21.30/21.32	2.11/2.44
	22.75/23.15	22.74/23.17	1.86/1.85	23.25/23.30	23.26/23.28	0.73/0.44
8 layers aniso./iso.	20.60/20.95	20.57/20.93	0.51/0.47	21.15/21.05	21.12/21.06	1.43/1.36
	22.90/23.30	22.89/23.28	1.04/1.00	23.50/23.45	23.50/23.43	0.46/0.47
	CNC (110) + GO-COOH			**CNC (110) + GO-OH**		
	***2θ* (°) (MD)**	***2θ* (°) (Analytical)**	**Intensity (10^8) (Analytical)**	***2θ* (°) (MD)**	***2θ* (°) (Analytical)**	**Intensity (10^8) (Analytical)**
20 layers aniso./iso.	22.70/22.35	22.70/22.36	1.75/8.63	22.90/22.45	22.88/22.43	2.24/1.12
	23.30/22.95	23.29/22.93	13.82/5.24	23.50/23.00	23.49/23.01	13.01/12.65
10 layers aniso./iso.	21.90/21.75	21.90/21.72	0.12/0.20	22.20/21.85	22.18/21.86	0.23/0.07
	23.00/22.80	22.98/22.79	3.64/3.64	23.30/22.95	23.29/22.93	3.51/2.52
7 layers aniso./iso.	-/-	21.43/21.25	0.01/0.00	-/-	21.73/21.39	0.03/0.07
	22.85/22.65	22.87/22.68	1.63/1.55	23.20/22.85	23.21/22.83	1.13/0.78

Table 3. 4: Comparisons between MD and analytical 2θ values as well as the analytical intensities (without corrections) of (200) peaks for all cases. The values before and after slash are under anisotropic and isotropic pressure controls, respectively.

given in Table 3. 3 and Table 3. 4.

As observed from the MD simulations, a non-uniform strain field within the CNC slab is developed due to the formation of hydrogen bonds at the CNC-GO interface. As shown in Figure 3. 8, the interface interaction between GO and CNC slab (200) facet can increase the distortion of the CNC lattice in *a*-*b* plane. However, it reduces the distortion of CNC lattice under the interface interaction between GO and CNC slab (110) facet. The lattice structure variation is more significant in the adjacent two layers at the CNC-GO interface than the layers inside the CNC slab. For example, in Figure 3. 8, the centers of masses of cellulose monomers of the sandwich structure CNC slabs (red and blue solid circles for GO-COOH and GO-OH, respectively) significantly deviate from those of the pristine CNC bulk (black open circles), within the adjacent two layers at the CNC-GO interface. The centers of masses from both pristine and sandwich structures overlap in the middle.

In order to quantify the distortion of the CNC lattice, we calculate the lattice parameters for both pristine CNC and sandwich structures. The lattice parameter variations with respect to the CNC orientation, the CNC thickness and the GO oxidation type are presented in Table 3. 3. It is found that the CNC (200) facet interaction with GO can enlarge the γ, and the interaction of the CNC (110) facet with GO can reduce γ. The GO with -OH functional groups (denoted as GO-OH) can lead more elongation of the cellulose along *a* direction compared to the GO with -COOH functional groups (denoted as GO-COOH). Although the elongation along *a* direction can trigger the (200) peak shift in the XRD spectrum, such elongation is not uniformly distributed. The local elongation near the CNC-

GO interface is much larger compared to the local elongation developed at the center domain of the CNC slab. The clear difference between the *d*-spacing near the CNC-GO interface and the *d*-spacing near the center of CNC slab lead to the bifurcation of the (200) peak, shown in Figure 3. 7 (a). Compared with the interaction between CNC (200) and GO-COOH, the interaction between CNC (200) with GO-OH brings larger $d_{(200)}$ variation at the center domain of the CNC (200). From equation (3.3), each 0.29±0.09 Å increase in $d_{(200)}$ can bring about a shift of 1.80±0.55° to the left in 2θ of the (200) peak in the XRD profile, and vice versa. Therefore, the enlarged $d_{(200)}$-spacing at the center domain of the CNC (200) when interacted with GO-OH can result in a high intensity (200) peak near 21° to 22°, shown as the blue lines in Figure 3. 7 (a). On the other hand, the (200) peak related with the center domain of CNC (200) when interacted with GO-COOH remains near 2θ =22.9º and shifts a little to the right with the decreasing CNC slab thicknesses, indicated by the red lines in Figure 3. 7 (a).

In order to further substantiate the non-uniform *d*-spacing distribution throughout the CNC slabs, the MD and analytical 2θ values (from Figure 3. 7 XRD spectra and equation (3.3), respectively) are tabulated in Table 3. 4 for comparison. By selecting proper integers for all Miller indices, the possible *d*-spacing values dominated at either near CNC-GO interface or the center domain are derived by equation (3.3). The 2θ values can be then calculated with the Bragg's Law. All splitting 2θ positions of the (200) plane are found through the calculations, which are in good agreement with those of the MD results. In conclusion, this analysis clearly shows that the CNC-GO interaction impacts the characteristics of its XRD spectrum. More specifically, when CNC slab is thin, the

corresponding strain field induced by CNC-GO interaction significantly affects the XRD spectra.

3.3.4 Discussion on XRD intensity

The intensity of the diffraction peaks is determined by the periodicity of the atomistic structure within the unit cell, which can be estimated through equations (3.4) and (3.5) [83],

$$F_{(hkl)} = \sum_n f_n \exp\left(2\pi i\left(hx + ky + lz\right)\right) \tag{3.4}$$

$$I_{(hkl)} \propto F_{(hkl)} \cdot F^*_{(hkl)} = \sum_{m=1}^{3}[(\sum_n f_m \sin(2\pi(hx+ky+lz)))^2 + (\sum_n f_m \cos(2\pi(hx+ky+lz)))^2] \tag{3.5}$$

where $F_{(hkl)}$ is the structure factor which can be determined by the Miller indices (*hkl*) and the fractional coordinates (*x*, *y*, *z*) over *n* atoms; f_n and f_m are atomic scattering factors determined by a 9-coefficient equation of Don Cromer and J. Mann [84]; $I_{(hkl)}$ is the crude peak intensity without correction factors, respectively. Through equations (3.4) and (3.5), the (200) peak intensities can be estimated, as shown in the third and the sixth columns of Table 3. 4.

For instance, for the cases of CNC/10 (200) interface with -COOH and -OH, as shown in Figure 3. 7 (a), -COOH case shows higher intensity at 22.75° but the lower intensity at 20.80° as opposed to the case of -OH. As discussed previously, the higher intensity of -COOH case at 22.75° is from the diffraction of the smaller *d*-spacing near the center domain, with the lower intensity at 20.80° caused by the weakening through more extensive conformational variations via the hydrogen bonds. In contrast, the -OH case has

a larger *d*-spacing near the center domain, with a barely discernible powder diffraction at 23.25°, which instead accumulates the intensity at 21.30°. Meanwhile, with a lower grade of disorganization at the interface, -OH case appears to have higher sum intensity from both 20.50° and 23.50° compared to the -COOH. In conclusion, the analytical intensity estimation without correction factors shown in Table 3. 4 is quantitatively well-matched with the XRD spectrum calculated from the MD simulation shown in Figure 3. 7.

The lattice parameters and (200) peak positions and intensities under isotropic pressure control are also given in Table 3. 3 and Table 3. 4. Combining the results from Table 3. 3 and Table 3. 4 with the peak shifting and weakening in Figure 3. 7, the difference between anisotropic and isotropic pressure controls can be clarified. For instance, from Table 3. 3, the lattice constant a and lattice angle γ of (200) GO-COOH sandwich structures under isotropic pressure control decrease faster than those under anisotropic pressure control as the CNC slab thickness reduces, there comes smaller *d*-spacing or bigger 2θ value for isotropic pressure control, thus the (200) peaks of -COOH under both pressure controls shift rightward and the isotropic peak diverges from the anisotropic peak, as shown in red lines in Figure 3. 7 (a). This is also consistent with the (200) peak position calculations as shown in the bottom row of each thickness for the (200) GO-COOH structure in Table 3. 4. The (1-10) and (110) peak shifting motion of (110) sandwich structures under these two pressure controls can be derived by plugging the varied lattice parameters to equation (3.3), and it reads that the (1-10) and (110) peaks shift towards each other, regardless of the pressure control. Comparing the relative peak intensities from Table

3. 4 column 3 and column 6 with those shown in Figure 3. 7, the difference between anisotropic and isotropic pressure control can be identified.

The hydrogen bond analysis that addresses the formation of the local and global non-uniform strain fields at the interface and over the lattice will be discussed in detail in Section 4.3.5.

3.4 Conclusions

We have observed in the experiment the suppression of CNC (200) facet intensity in the XRD spectrum of CNC-GO nanocomposites with the use of highly crystallized CNC and highly oxidized single-to-few-layer GO, and numerically we have identified the mechanisms with the use of crystallography behind such facet manipulation through MD simulation. We have reached the following conclusions:

(1) The hydrogen bonds at the CNC-GO interface induce a non-uniform strain field to the CNC structure, including a global strain throughout the CNC slab and a local strain near the CNC-GO interface.

(2) The interaction at (200) CNC-GO interface largely causes the broadening and weakening of the (200) peak. The interaction at (110) CNC-GO interface enhances the intensity of (1-10)/(110) peaks since the two peaks tend to shift closer to each other.

(3) The isotropic and anisotropic pressure controls yield different peak XRD positions and intensities of three major planes due to different sets of lattice parameters. However, they both yield the identical trends stated in (2).

IV. HYDROGEN BONDS IMPACT ON THE INTERFACE MORPHOLOGICAL VARIATIONS OF THE CNC-GO NANOCOMPOSITES

4.1 Motivation

In Chapter III, we have investigated the impact of CNC-GO interface interaction on the peak shifting and peak widening of the XRD spectrum with respect to the CNC slab thickness, orientation and GO oxidation type. The hydrogen bonds at the CNC-GO interface induce a non-uniform strain field to the cellulose structure, including a global strain field throughout the CNC slab and a local strain field near the CNC-GO interface. In Chapter IV, we will systematically investigate the morphological variations of the CNC-GO sandwich structure near the interface and the hydrogen bond effects behind it.

4.2 Modeling Setups

We use the similar modeling setup as presented in Chapter III. The thicknesses of CNC slab in Chapter IV only include 20-layer and 10-layer. The timestep size is 0.5 fs. The temperature is set to be 100 K in order to suppress the thermal fluctuation noise and focus on the hydrogen bonding effects on the interface morphological variations. After the supercell reaches its equilibrium condition under the isothermal-isobaric (NPT) ensemble, 650 ps relaxation data are then recorded for the subsequent statistical investigations unless it is specified separately in the following content.

As discussed in Chapter III, the isotropic and anisotropic pressure controls yield different lattice parameters and different XRD peak positions of three major planes. The

objective of the investigation in Chapter IV is to elucidate the degree of morphological variations of the sandwich structures induced by the CNC-GO interface compared to the pristine CNC structure without any preexisting stress. Thus, the anisotropic pressure setup is employed, which means the three dimensions are not coupled and change independently in accordance with the pressure components. Since the morphological variations of sandwich structures under isotropic pressure control entail the interference from preexisting stress, we only address the comparison between anisotropic and isotropic pressure controls for pristine CNC structure with respect to the aspects of interest.

4.3 Results and Discussion

4.3.1 Three Levels of Rotations

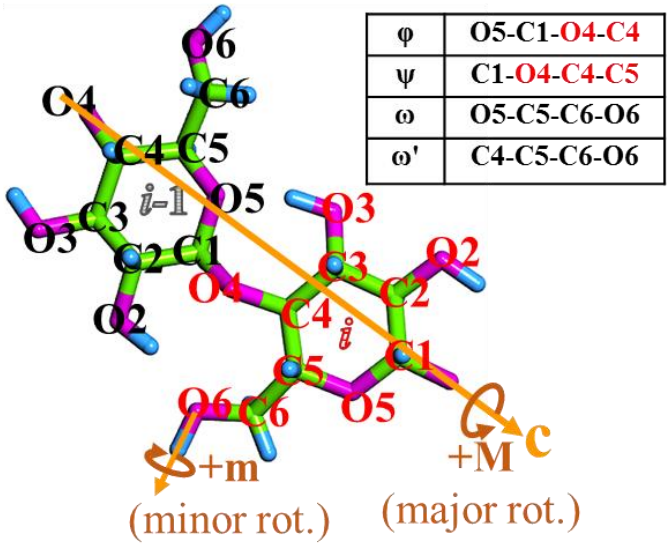

Figure 4. 1: The morphological variations of Iβ CNC, including the major rotation +M (glucose torque about axis c), minor rotation +m (the terminal hydroxyl groups flipping), and the intermediate rotations (the variations of the dihedral angles φ and ψ of backbones between two glucose rings (i and i-1), and those of the dihedral angles ω' and ω of side chains in glucose rings).

Regarding the CNC-GO interaction at the interface, the morphological variations of the CNC slab mainly locate at the first two layers next to the GO plane. As illustrated in

Figure 4. 1, we define the major rotation as the torsion of the glucose ring about the axial direction *c*; the intermediate rotations as the relative rotation of consecutive two glucose rings and the relative rotation of the glucose ring and its side chain -CH_2-OH; and the minor rotation as the flipping motion of the hydrogen atom on the -OH/-CH groups with respect to the CNC surface orientation.

4.3.2 Major Rotation: Glucose Ring Twisting

The major rotation defined in Figure 4. 1 reflects the twisting of the glucose ring as one unit to the axis of the backbone (*c* axis). Each anhydroglucose ring includes six carbon atoms (C1~C6) and one oxygen atom (O6). The torque $\mathbf{M}_n(t)$ of an anhydroglucose ring *n* with respect to the axis *c* at the timestep *t* is defined as $\mathbf{M}_n(t)=\sum_{i=1}^{7}\mathbf{r}_i^n(t)\times\mathbf{F}_i^n(t)$, where $\mathbf{r}_i^n(t)$ is the distance vector from *c* axis to the atom *i* in the anhydroglucose ring *n*, and $\mathbf{F}_i^n(t)$ is the force vector of the atom *i* in the anhydroglucose ring *n*. For the sandwich structure, the mean torque variation of the anhydroglucose ring *n* due to the CNC-GO interface interaction is calculated by $\overline{\Delta\mathbf{M}}_n=\frac{1}{N_t}\sum_{t=1}^{N_t}\left(\mathbf{M}_n(t)-\mathbf{M}^0\right)$, where $\mathbf{M}^0$ is the reference torque obtained from the relaxed pristine CNC structure, and N_t is the number of timesteps. In the relaxed pristine CNC structure, the stable anhydroglucose ring tends to be in the chair conformation with an average net torque to be zero. Taking a 10-layer pristine CNC structure of (200) orientation (CNC/10 (200) as an example, Figure 4. 2 (a) presents the averaged torque $\mathbf{M_n}$ of each anhydroglucose ring on one (200) layer with respect to a time period of 300 ps. Even though the average torque $\mathbf{M_n}$ on each ring is not

zero, they all fluctuate around zero. Figure 4. 2 (b) presents the torque statistics of all 500 anhydroglucose rings within 10 layers of the relaxed pristine CNC structure with respect to time and position over a time period of 300 ps. It shows the average torque μ is zero, but the standard deviation σ is ~74.6 kcal/mol. It proves that 300 ps is a sufficient time period to collect enough data for the reference torque calculation. On the other hand, the fluctuation of the torque with respect to time is significant. Figure 4. 2 (c) presents the

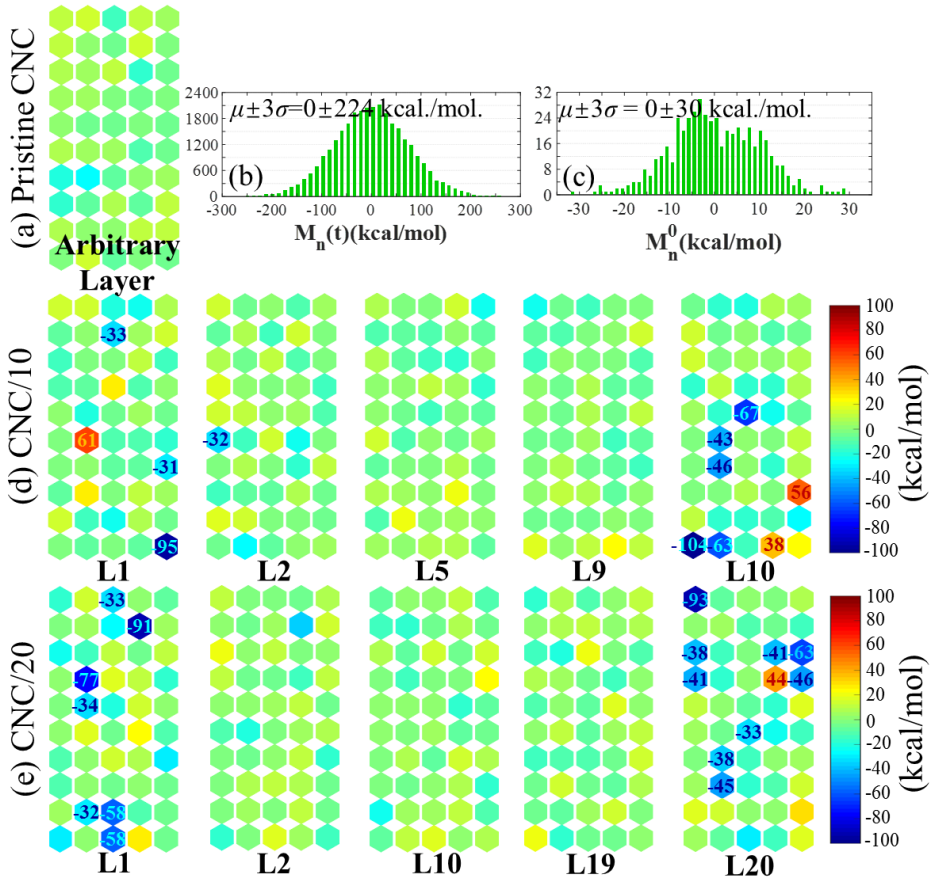

Figure 4. 2: (a) The average torque over timestep for an arbitrary (200) plane in the pristine CNC; (b) the torque statistics with respect to time and position in the pristine CNC; (c) the reference torque statistics with respect to position in the pristine CNC; (d) the average torque distribution at selected layers of CNC (200) slab of 10-layer thickness (denoted as CNC/10) when interacting with GO-COOH; (e) the average torque distribution at selected layers of CNC (200) slab of 20-layer thickness (denoted as CNC/20) when interacting with GO-COOH.

average torque (with respect to time) statistics of all 500 anhydroglucose rings with respect to position. It shows the standard deviation σ is reduced to 10 kcal/mol. We believe with the increasing length of time period, such standard deviation can be further reduced.

In the following analysis, we define the reference torque $\mathbf{M}^0$ to be zero and treat $\overline{\Delta \mathbf{M}}_n \in [-30 \quad 30]$ kcal/mol. as normal fluctuation with respect to a time period of 300 ps. In order to understand the effect of CNC-GO interface interaction on the anhydroglucose ring twisting near the CNC-GO interface, we investigate the mean torque variation of the anhydroglucose ring at different layers of the CNC-GO sandwich structure. For example, Figure 4. 2 (d) and (c) present the average torque variations of anhydroglucose rings at selected layers of CNC (200) slab of 10-layer and 20-layer thicknesses when interacting with GO-COOH. The average torque variations which exceed the normal fluctuation range are highlighted by their magnitude. For 10-layer and 20-layer thicknesses (denoted as CNC/10 and CNC/20, respectively), the major rotation with abnormal torques is observed on some of the anhydroglucose rings at the first nearest layers (L1, L10 for CNC/10 and L1, L20 for CNC/20, respectively). Such phenomena can hardly be observed at the layers away from the CNC-GO interface. The average torque fluctuation at the middle layer of the CNC slab (L5 in Figure 4. 2 (d) and L10 in Figure 4. 2 (e)) is similar to that of the pristine CNC (Figure 4. 2 (a)).

4.3.3 Intermediate Rotations: Dihedral Angle shifting

The intermediate rotations define the rotation between consecutive two glucose rings and the rotation between the glucose ring and its side chain -CH_2-OH. The rotation between two glucose rings can be examined by the variations of dihedral angles φ and ψ.

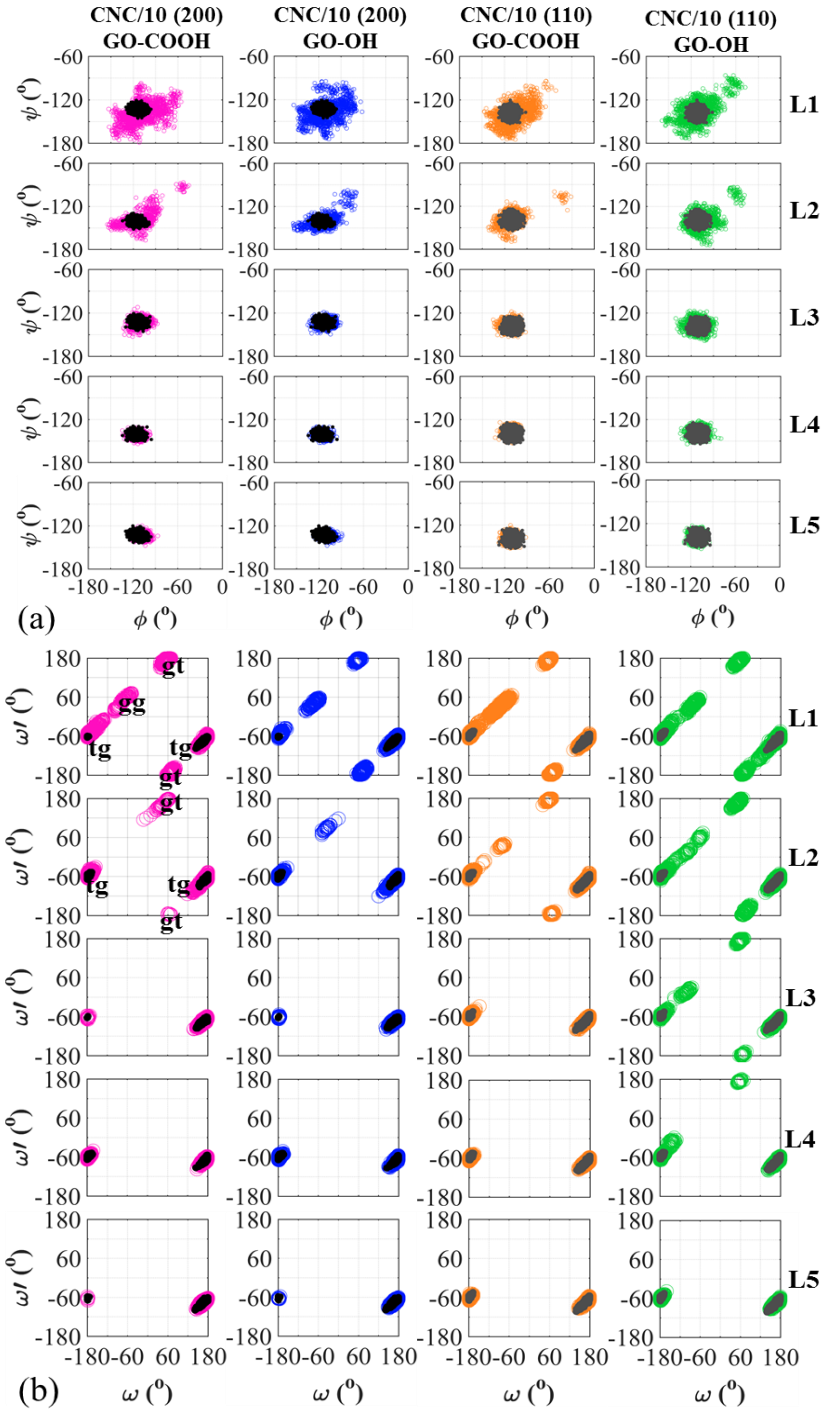

Figure 4. 3: (a) Dihedral angle ψ - φ distribution; (b) dihedral angle ω' - ω distribution with respect to the CNC slab orientation, and the GO oxidation type for sandwich structures of 10-layer thickness. L1→L5 represent the layers from the interface to the middle of CNC slab. Black and grey solid dots represent the dihedral angle distributions of the (200) and (110) pristine CNCs at the relaxed states.

The rotation between the glucose ring and the attaching side chain can be examined by the

variations of dihedral angles ω and ω', respectively.

Figure 4. 3 (a) gives the ψ - φ distributions of CNC/10 (200) and CNC/10 (110) structures of layers L1 to L5 from top to bottom. From left to right, the ψ - φ distributions of CNC/10 (200) GO-COOH, CNC/10 (200) GO-OH, CNC/10 (110) GO-COOH, and CNC/10 (110) GO-OH are presented in pink, blue, orange and green open circles, respectively. As the reference, the ψ - φ distributions of the pristine CNCs are also presented. For pristine CNCs, the ψ - φ distributions are relatively concentrated in a round (CNC/10 (200)) or elliptical (CNC/10 (110)) region within $\varphi \in$ (-150°, -90°) and $\psi \in$ (-180°, -120°), which presents a stable low energy basin of Iβ CNC structure. However, regardless of the CNC facet orientation and the GO oxidation type, the ψ - φ distributions of CNC are significantly disturbed at the first two layers near the CNC-GO interface. Meanwhile, the ψ - φ distributions of CNC at the middle layers of the CNC slabs remain undisturbed. More interestingly, there exists a separate basin at $\varphi \in$ (-75°, -35°) and $\psi \in$ (-115°, -85°) (a different stable conformation) at L1 and L2 of CNC/10 (110), regardless of the GO oxidation type. A similar basin at $\varphi \in$ (-100°, -45°) and $\psi \in$ (-125°, -85°) only appears at the L2 for CNC/10 (200), regardless of the GO oxidation type. Additionally, the separate basins of GO-COOH structures are farther from the major basins compared to that of the GO-OH structures. This implicates the higher polarity of -COOH groups, which twists the backbone dihedral angles more intensively. As shown in Figure 3. 3 (a), the L1 and L2 layers of CNC/10 (200) are origin and center chain layers, respectively. Since the origin chain layer is more stable than the center chain layer due to the rotation of the origin

chains relative to (200) plane, it is harder to be altered as directly exposed to the interface, so that the separate basins in L1 of CNC/10 (200) structures are missing. We also find that the ψ - φ distributions of CNC/10 (200) at L10-layer (center chain layer) have such separate basins while L9 layer (origin chain layer) does not. The inter-planar hydrogen bonds hinder the origin chain layers from being altered with a relatively high-energy barrier. On the other hand, all layers of CNC (110) structures are mixed with both types, which contributes to the noticeable separation at the first two layers of the CNC near the CNC-GO interface. The previous investigation on ψ - φ distribution has been experimentally conducted with respect to temperature dependence [85][86]. The major basin at $\varphi \in$ (-150°, -90°) and $\psi \in$ (-180°, -120°) roughly corresponds to the low-temperature condition. With rising temperature, other basins connected to or separated from the major one are gradually populated over time. The rising temperature has a similar effect on the backbone dihedral angle ψ - φ variations of the CNC when interacting with the GO.

Figure 4. 3 (b) gives the ω'- ω distributions of CNC/10 (200) and CNC/10 (110) structures of layers L1 to L5 from top to bottom. From left to right, the ω'- ω distributions of CNC/10 (200) GO-COOH, CNC/10 (200) GO-OH, CNC/10 (110) GO-COOH and CNC/10 (110) GO-OH are presented in pink, blue, orange and green open circles, respectively. The ω'- ω distributions of the pristine CNCs are plotted as well. Two letter code is employed to describe the three energetically favored conformations of dihedral angles ω'and ω. The first letter specifies the position of the O6 atom as either trans or gauche with respect to the O5 atom, and the second letter specifies its relationship to the

C4 atom. In Newman projections, trans means one half of the backbone continuing on either side of a C5-C6; gauche means both halves on the same side, with gauche+ clockwise and gauche- counterclockwise rotating to the other half from the trans position. Here, "*gg*" represents ω in gauche+ and ω' in gauche-, "*gt*" represents ω in gauche- and ω' in trans, and "*tg*" represents ω in trans and ω' in gauche+ [85][87][88]. In the pristine CNC structure, only "*tg*" conformation can be observed [29]. However, in the CNC-GO sandwich structure, the dihedral angles ω'-ω are significantly altered, especially near the CNC-GO interface. In the vicinity of the (200) CNC-GO interface, two new conformations "*gg*" and "*gt*" are identified at the first nearest layer L1, regardless of the CNC slab thickness and the GO oxidation type. Interestingly, the second nearest layer of CNC/10 (200) GO-COOH shows "*gt*" but no "*gg*" conformation, and that of CNC/10 (200) GO-OH exhibits "*gg*" but no "*gt*" conformation. Moreover, despite the mixture of "*gt*" and "*gg*" in the second layer of CNC/10 (110), GO-COOH structure presents fewer "*gg*" conformations than the GO-OH structure. It is found that "*gg*" conformation of pristine CNC (200) surface is the most populated in aqueous solution or at high temperature with the lowest free energy, followed by "*gt*", whereas "*tg*" is the least populated [88][89][90]. As the transition layer between the direct interface and middle layers, the second nearest layer (L2) has its special hydrogen bonding networks that favor either pure "*gt*" or pure "*gg*" or the combination, depending on the oxidation type of GO and CNC facet orientation. The ω'-ω distributions of L5 remain undisturbed compared to that of the pristine CNC, since these layers are far beyond the interface impact.

The black and grey dot references of ω'-ω distributions in Figure 4. 3 (b) are the pristine CNCs of (200) and (110) orientations under anisotropic pressure controls, respectively, where only the "*tg*" conformation exists. This conformation has been observed to be dominant in native Iβ CNC at the dry environment. It was first proposed by

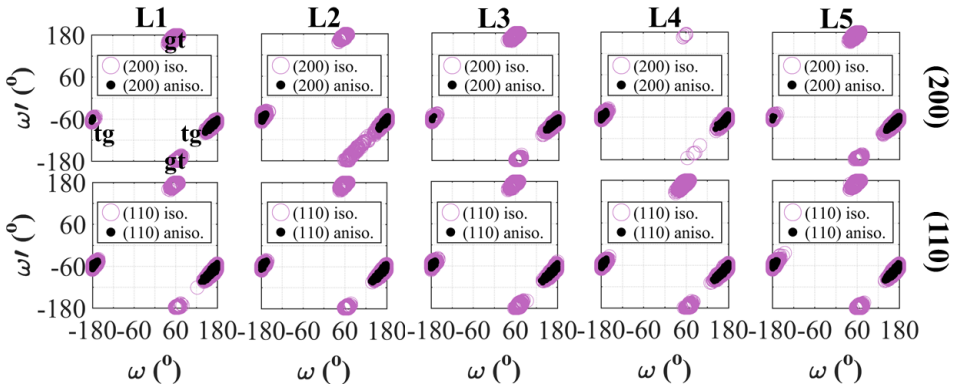

Figure 4. 4: Dihedral angle ω'-ω distributions for pristine CNCs under isotropic and anisotropic pressure controls. The top and bottom rows are pristine CNCs of (200) and (110) orientations, respectively. The black solid dots and purple circles represent the dihedral angle distributions under anisotropic and isotropic pressure controls in the equilibrium state, respectively.

linked atom structure refinement via X-ray diffraction data [91] and later verified by the empirical relationship between ^{13}C NMR chemical shift of C6 and its conformation [92]. More recently, the oxygen atom O6 of hydroxymethyl group in "*tg*" conformation was visualized in Fourier omit map via high-resolution X-ray diffraction data [29]. In Figure 4. 4, the ω'-ω distributions of pristine CNCs of (200) and (110) orientations under anisotropic and isotropic pressure controls are graphed. Both "*tg*" and "*gt*" conformations appear regardless of the orientation, as the isotropic pressure control is applied to. The appearance of "*gt*" conformation under isotropic pressure control is obviously unphysical, and meanwhile we have observed at least 50 % of CNC chains in the bulk transform from its original crystalline state to a disordered state.

4.3.4 Minor Rotation: Hydrogen Flipping of -CH and -OH

The minor rotation captures the hydrogen flipping dynamics of -CH and -OH terminal groups on the CNC chains. Flipping in→out is defined as hydrogen atoms pointing towards the GO interface from its initial state which is against the GO interface, and vice versa for flipping out→in.

Before we start to discuss the hydrogen flipping of -CH and -OH of CNC chains as they are in contact with GO with respect to the CNC slab orientation, CNC slab thickness and GO oxidation type, we first present the comparison between isotropic (dark and light purple symbols) and anisotropic (black and grey symbols) pressure controls for the pristine CNCs of (200) and (110) orientations. In Figure 4. 5 (a), pristine CNC under anisotropic control has little difference of both -CH and -OH flipping dynamics between origin and center chain layers, whereas that under isotropic pressure control has more -CH hydrogen flipping in the origin chain layers and more -OH hydrogen flipping in the center chain layers. The balance between flip in→out and out→in is maintained for both pressure controls. In Figure 4. 5 (b), the -CH and -OH hydrogen flipping dynamics of anisotropic pressure control stays stable throughout all layers and there is also little difference between flip in→out and out→in. Unlike the straight-line pattern of anisotropic pressure control, the -CH hydrogen flipping at L1 and L10 of isotropic pressure control gets close to the corresponding points of anisotropic pressure control, whereas as going to the middle layers, the -CH hydrogen flipping deviates from the lines of anisotropic pressure control. The -OH hydrogen flipping generally follows the similar trend with bigger standard deviation.

This bridge-like distribution of (110) orientation under isotropic pressure can be attributed to the equilibrium microstructure, as shown in Figure 4. 5 (c).

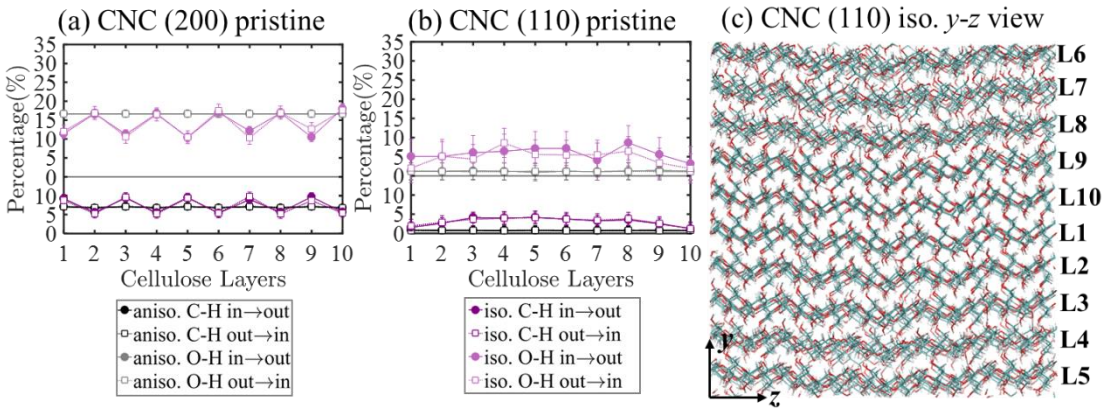

Figure 4. 5: Hydrogen flipping of -CH and -OH terminal groups for (a) pristine CNC of (200) orientation under isotropic and anisotropic pressure controls; (b) pristine CNC of (110) orientation under isotropic and anisotropic pressure controls. (c) The y - z plane view of pristine CNC microstructure of (110) orientation under isotropic pressure control. All CNC structures are under PBC. For (200) orientation, odd layers are origin chain layers, and even layers are center chain layers, respectively.

Figure 4. 6 (a) shows the hydrogen atom flipping of -CH and -OH on CNC surface with respect to the CNC slab orientation, CNC slab thickness and GO oxidation type. Hydrogen atoms attached to carbon atoms (-CH) are maintained and balanced regardless of the CNC slab orientation and the GO oxidation type. The CNC-GO interface interaction will slightly increase the hydrogen flipping dynamics near the interface, but the balance between flip in→out and out→in is well maintained. This is because -CH is essentially a nonpolar group, which has little sensitivity to the presence of GO.

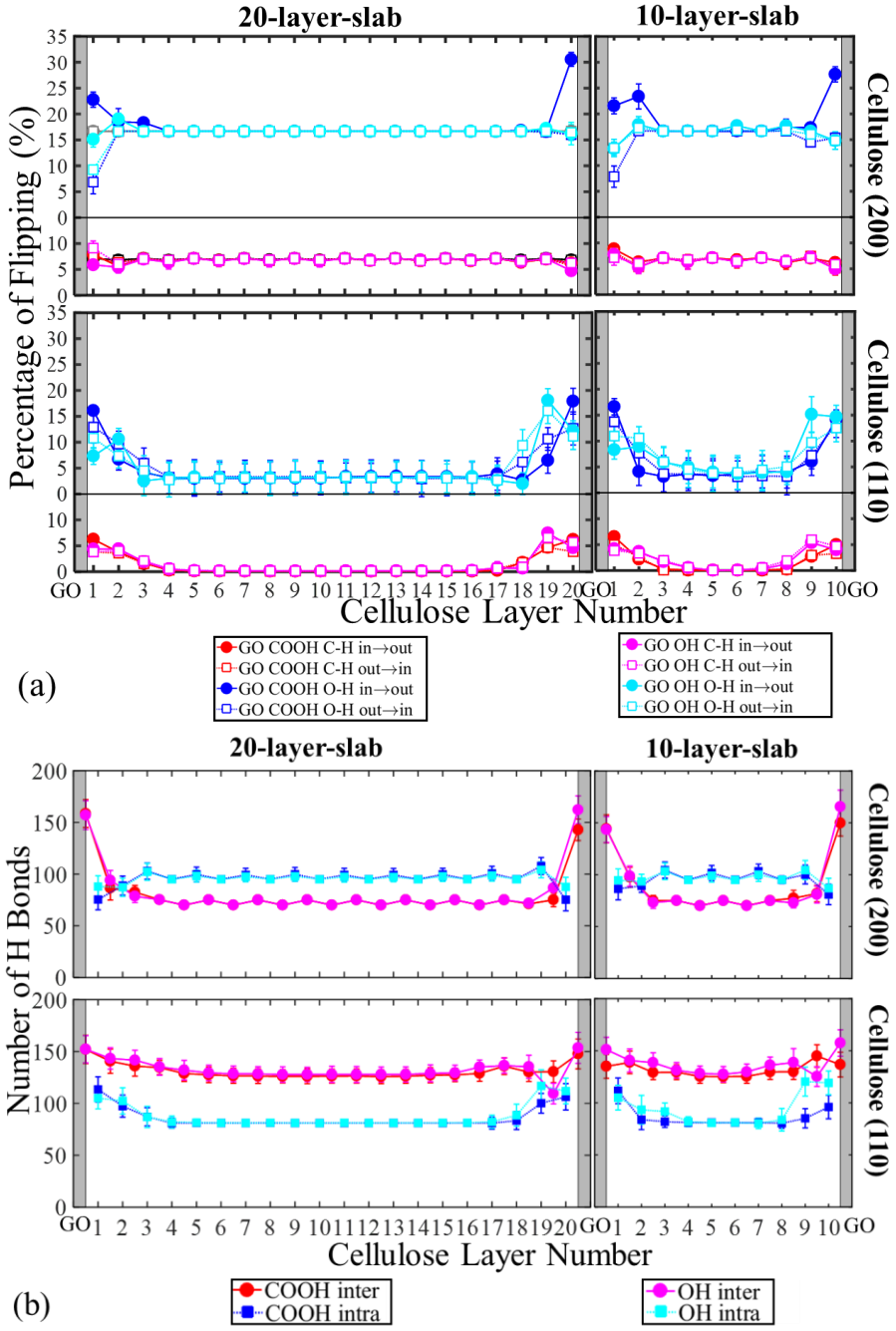

Figure 4. 6: (a) Hydrogen flipping of -CH and -OH groups and (b) hydrogen bond number variations with respect to the CNC slab thickness, orientation, and GO oxidation. From left to right, there are 20-layer-slab and 10-layer-slab structures, respectively. In the subfigures (a) and (b), the top row is of (200) orientation, while the bottom row is of (110) orientation. For all (200) orientation structures, odd layers are origin chain layers, and even layers are center chain layers, respectively.

However, for the hydrogen atoms that belong to the hydroxyl groups (-OH), the

flipping dynamics is significantly affected by the interaction at the CNC-GO interface and substantially depends on the CNC slab orientation and the GO oxidation type, as the blue and cyan symbols shown in Figure 4. 6 (a) for CNC (200) and (110) layers, respectively. For the CNC (200) interfaces, the -OH flipping dynamics of the CNC slab is not affected near the middle layers of the CNC slab, but significantly disturbed near the CNC-GO interface, regardless of the slab thickness. Moreover, the balance of -OH flipping is totally broken near the CNC-GO interface when CNC (200) plane interacts with GO-COOH, as the blue symbols shown in the top row of Figure 4. 6 (a). The percentage of the -OH hydrogen flipping in→out (solid blue circle) is much higher than that of the -OH hydrogen flipping out→in (hollow blue square) due to the hydrogen bond formation between -OH groups on CNC and -COOH groups on GO at the interface. The difference between -OH flipping in→out and out→in is around 15 %, which is significant compared to the normal -OH flipping percentage (16 %). This observation brings the fact that the GO oxidation type can be utilized to specifically alter the conformation of -OH on CNC (200) surface.

For the CNC (110) interfaces, the -OH flipping dynamics of the CNC slab is affected throughout the CNC slab thickness with a 2 % increase. It is because the inter-plane and intra-plane hydrogen bonding networks within the CNC lattice are disturbed due to the global strain brought by the (110) CNC-GO interaction [8]. Y. Li *et al.* [88] reported that the abundant hydroxyl groups in nanofibrillated cellulose of the nanopaper significantly increase the hydrogen bonds between the neighboring GO sheets. R. Alqus *et al.* [16] also mentioned the similar phenomenon as the cellulose (200) plane is in contact with graphene in the aqueous solution. Near the CNC-GO interface, a higher impact up to

15 % increase appears at the first three layers of the CNC, regardless of the CNC slab thickness and the GO oxidation type. However, the -OH hydrogen flipping balance is well maintained. This is because -OH group is a polar group, which is sensitive to the interaction at the CNC-GO interface due to the formation of hydrogen bonds. All the -OH groups on (110) plane are directly exposed to the interaction plane (either another layer of CNC (110) plane or the GO plane). Hence, there is less possibility for the -OH groups to make a huge difference between flip in→out and out→in. Therefore, the flipping dynamics of CNC (110) interfaces is affected near the CNC-GO interface but remains balanced.

To better understand the local and global non-uniform strain fields at the CNC-GO interface and over the entire lattice, that disturb the periodicity and cause peak weakening and shifting, as shown in Figure 3. 7, we can inspect the results in Figure 4. 6 (a) and identify the difference of -CH and -OH flipping dynamics between flipping in→out and out→in, and thus may find the causation for the above observations. As shown in Figure 4. 6 (a), for the hydrogen atoms attached to carbon atoms (-C-H), their flipping dynamics is maintained and balanced, regardless of the oxidation type on the GO and the orientation of the CNC slab surface. However, for the hydrogen atoms on hydroxyl groups (-O-H), the interaction at the GO and CNC slab greatly affects the flipping dynamics, which significantly depends on the functional groups on GO and CNC slab orientations. When the CNC slab (200) facet interacts with the carboxyl groups (-COOH) on GO, the flipping dynamics of hydrogen on the adjacent two layers of CNC (200) slab at the CNC-GO interface is unbalanced. More hydroxyl groups that are initially under the surface are flipped out to interact with the carboxyl groups on GO. Therefore, the periodicity of the

atomistic structures along the (200) plane is no longer maintained. Combining with the discussion on peak weakening in Table 3. 4, the main reason responsible for (200) weakening shown as the magenta and red lines in Figure 3. 7 is revealed.

4.3.5 Hydrogen Bond Analysis

We have presented the morphological variations of the CNC at the CNC-GO interface, in the way of three rotations: major, intermediate and minor. It is obvious that the interaction at the CNC-GO interface only brings the major rotation for the CNC anhydroglucose rings mainly at the first nearest layer, regardless of the CNC slab orientation and the GO oxidation type. However, the CNC-GO interface interaction greatly impacts the minor rotation of the CNC, which is very sensitive to the CNC slab orientation and GO oxidation type. Since the majority of the CNC-GO interface interaction is induced by hydrogen bonds, it is of great importance to thoroughly investigate the hydrogen bond formation at the CNC-GO interface to substantiate the observations in the previous section. In the following, the inter-plane hydrogen bonds are defined as the hydrogen bonds between CNC/CNC planes and CNC/GO planes. The intra-plane bonds are defined as the hydrogen bonds within the CNC planes. The numbers of inter-plane and intra-plane hydrogen bonds are collected based on the H-A (donor hydrogen-acceptor oxygen) cutoff distance of 2.8 Å, and the D-H-A (donor oxygen-donor hydrogen-acceptor oxygen) angle of more than 110° [29][91].

We first address the comparison between isotropic and anisotropic pressure controls for the pristine CNCs of (200) and (110) orientations. Figure 4. 7 (a) shows more intra-plane than inter-plane hydrogen bonds for pristine CNC of (200) orientation under

anisotropic pressure control, yet more inter-plane than intra-plane hydrogen bonds for that under isotropic pressure control, which can be visualized through Materials Studio 8.0 [93]. This is because the hydroxymethyl groups under isotropic pressure control tend to flip towards the hydroxyl groups from the adjacent layers, so that inter-plane hydrogen bonds form, while intra-plane hydrogen bonds diminish. Accordingly, this transformation gives rise to the appearance of the new conformation "*gt*", shown in the top row of Figure 4. 4.

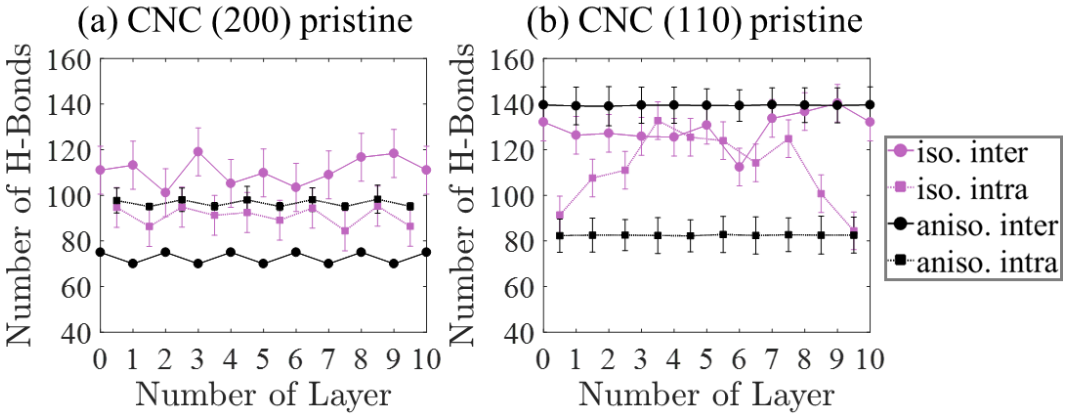

Figure 4. 7: Hydrogen bond variations for (a) pristine CNC of (200) orientation under isotropic and anisotropic pressure controls; (b) pristine CNC of (110) orientation under isotropic and anisotropic pressure controls. The black and purple symbols represent the isotropic and anisotropic pressure controls, and round and square symbols represent inter-plane and intra-plane hydrogen bonds, respectively. For (200) orientation, odd layers are origin chain layers, and even layers are center chain layers, respectively.

In Figure 4. 7 (b), there are more inter-plane than intra-plane hydrogen bonds for pristine CNC of (110) orientation under anisotropic pressure control, whereas the inter-plane and intra-plane hydrogen bond distributions are very similar to the -CH and -OH hydrogen flipping distributions under isotropic pressure control, as shown in Figure 4. 5 (c), i.e., the distributions at L1 and L10 are close to those under anisotropic pressure control due to the crystalline microstructure, but L3~L8 deviate from the anisotropic trend. Since L3~L8 as

shown in Figure 4. 5 (c) are disordered, the bridge-like distributions in both inter-plane and intra-plane hydrogen bonds appear.

Figure 4. 6 (b) presents the hydrogen bond number variations with respect to the CNC slab orientation, CNC slab thickness and GO oxidation type. For CNC (200) structures, the number of hydrogen bonds is greatly affected by the CNC-GO interaction up to the third layer of the CNC near the interface. The small up-and-down alternating pattern in the middle layers is due to the alternating spatial arrangement of origin and center chain layers of the CNC (200) slab. Compared to the pristine CNC, this alternating pattern is reversed with the introduction of GO at the CNC-GO interface. For the CNC (110) case, the distribution of inter-plane hydrogen bonds is affected throughout the CNC slab thickness due to the CNC-GO interface interaction. Compared with the pristine CNC structure, fewer inter-plane hydrogen bonds are formed at the middle layers, while more inter-plane hydrogen bonds are generated near the CNC-GO interfaces. On the other hand, the distributions of the intra-plane hydrogen bonds are only affected at the first three CNC layers near the CNC-GO interface. The hydrogen bond distributions near the middle layers are not affected.

The hydrogen bonds between CNC functional groups and GO functional groups mainly induce the strain field and morphological variations in the CNC lattice, that further affect the intensity of the associated XRD spectra. Recall that when the -OH groups of CNC face GO, their attached hydrogens can be easily trapped by the oxygen from -OH/-COOH groups on GO to form the hydrogen bonds. It is obvious that when CNC (200) facet interacts with GO in Figure 4. 6 (b), the inter-layer hydrogen bonds are significantly

redistributed between layers due to the CNC-GO interaction, regardless of the functional group type on GO. The number of inter-layer hydrogen bonds increases dramatically at the CNC-GO interface, while constantly reduces in the middle layers. However, the number of intra-layer hydrogen bonds remains undisturbed within each (200) plane of the CNC throughout the slab thickness. When CNC (110) facet interacts with GO, the numbers of inter-layer/intra-layer hydrogen bonds gradually increase when approaching to the CNC-GO interface. The number of intra-layer hydrogen bonds reduces significantly at the middle layers of the CNC slab, while the number of inter-layer hydrogen bonds at the middle layers only declines a little. Because of the surface orientation, the (200) peak weakening in Figure 3. 7 results from the inter-layer hydrogen bonds when CNC (200) facet interacts with GO, and the intra-layer hydrogen bonds when CNC (110) interacts with GO, which is consistent with our observation in Figure 4. 6 (a). For example, the extensive new formation of inter-layer hydrogen bonds near the (200) CNC-GO interface causes the conformation change in rotamers [87] and alternates the glucose rings' twisting, which can weaken the (200) peak intensity.

It is obvious that the hydrogen bond formation and redistribution are strongly correlated with the -OH flipping observed in Figure 4. 6 (a). Figure 4. 8 presents a schematic diagram of the hydrogen bond formation at the CNC-GO interface with respect to one glucose ring. For instance, when the -OH terminal group on cellulose serves as D-H (donor oxygen and donor hydrogen), such as the hydrogen bonds ①, ②, and ③, shown in Figure 4. 8, the hydrogen atoms on -OH terminal groups tend to flip out of the plane.

The amount of -OH flipping occurred at the nearest CNC layers is correlated with the D-H pairs from it.

Taking the 10-layer-slab sandwich structure as an example, the D-H number and type analysis of the inter-plane hydrogen bonds formed at the CNC-GO interface (L1 and L10 in Figure 3. 3 (a) and (b)) with respect to the CNC slab orientation and the GO oxidation type are performed, as shown in Figure 4. 9. As one -OH pair can serve multiple times as D-H with respect to different acceptors [94][95][96], the unique count for the D-H number is collected without counting the repeated elements. Such a unique count of the

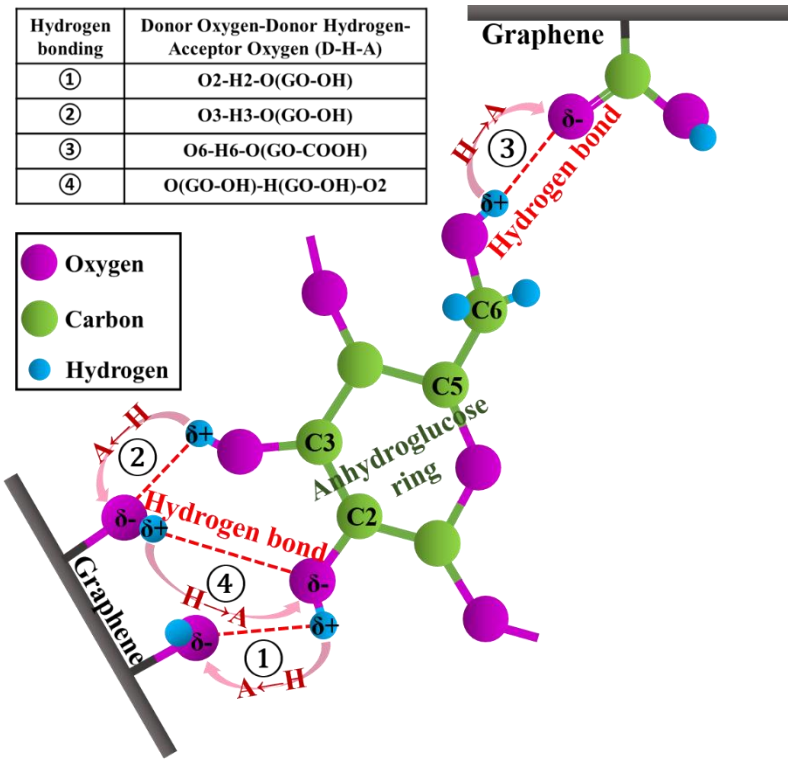

Figure 4. 8: The schematic diagram of hydrogen bond formation between the glucose ring of the CNC and GO planes. The representative D-H-A (donor oxygen, donor hydrogen, acceptor oxygen, respectively) relations are listed in the table. All types of D-H from the CNC slab can be categorized as O2-H2(①), O3-H3(②) and O6-H6(③), respectively. D-H types can be also found in GOs, such as ④. δ+ and δ- represent partial positive and negative charges due to unshared pairs of electrons. H→A represents the vector of donor hydrogen to acceptor oxygen.

inter-plane hydrogen bonds between pristine CNC (200) planes and (110) planes are

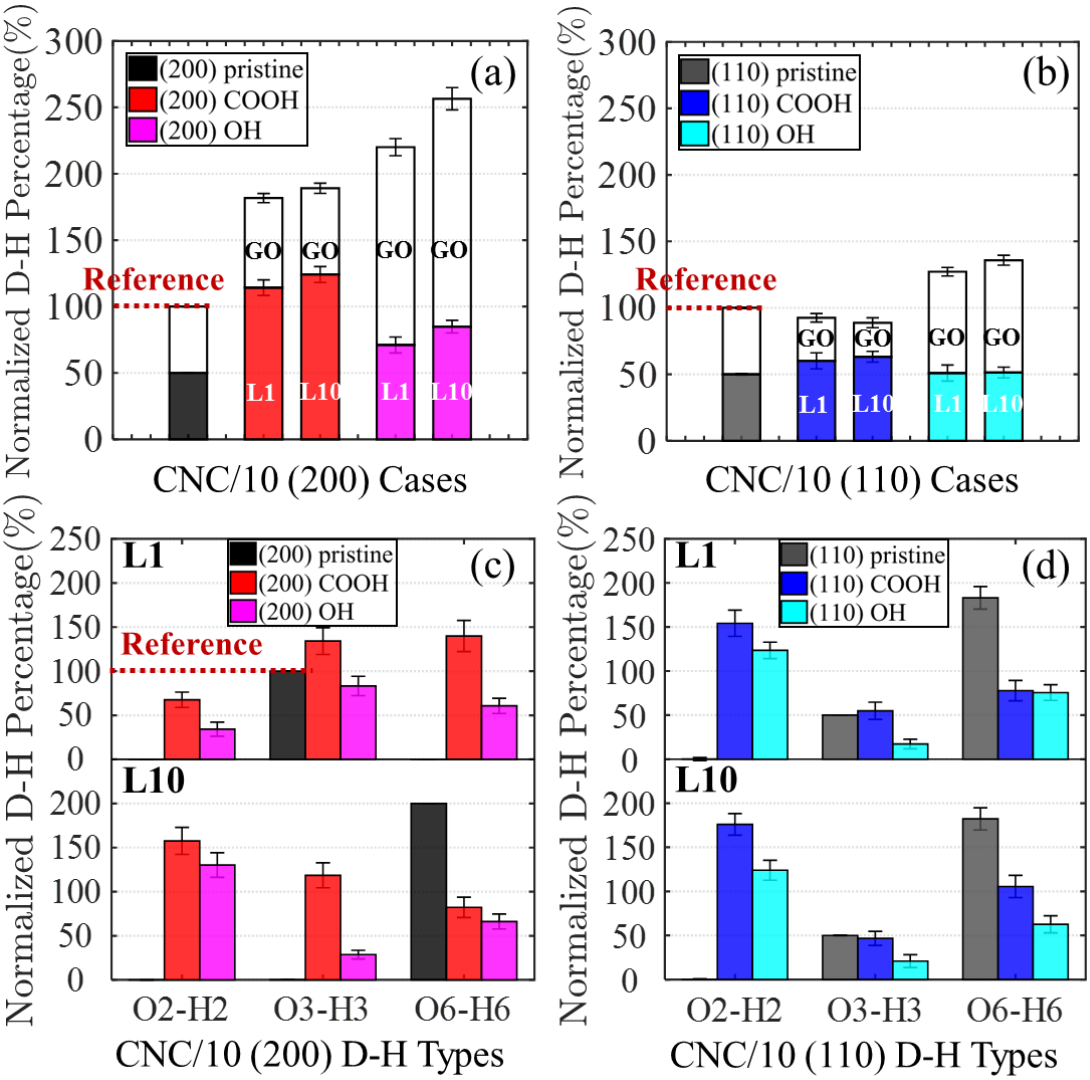

Figure 4. 9: D-H distribution with respect to the CNC slab orientation and GO oxidation type based on the 10-layer sandwich structures: (a) Normalized unique donor percentages at the interface of between pristine CNC/10 (200) plane and pristine CNC/10 (200), GO-COOH and GO-OH, respectively; (b) normalized unique donor percentages at the interface between pristine CNC/10 (110) and pristine CNC/10 (110), GO-COOH and GO-OH, respectively; (c) normalized donor percentages for D-H assignments of O2-H2, O3-H3 and O6-H6 for all CNC/10 (200) structures; and (d) normalized donor percentages for D-H assignments of O2-H2, O3-H3 and O6-H6 for all CNC/10 (110) structures. All percentage values are averaged with error bars. We normalize the counts by regarding unique D-H pairs of CNC/10 (200) pristine as 100 % (the sum of the first black and white bars in Figure 4. 9 (a)), and we normalize the counts by regarding D-H of O3-H3 type in L1 of CNC/10 (200) pristine as 100 % (the black bar on top of Figure 4. 9 (c)).

plotted, respectively. Adopting the total number of inter-plane hydrogen bonds of the pristine CNC as the normalization reference (100 %), Figure 4. 9 (a) and (b) present the normalized number of D-H pairs on each side of the interaction interface with respect to the CNC slab orientation and GO oxidation type. Apparently, the introduction of CNC-GO interaction considerably increases the number of inter-plane hydrogen bonds at the (200) CNC-GO interface (GO-L1 and L10-GO, respectively), shown in Figure 4. 9 (a). The -OH oxidation type on GO can bring more hydrogen bonds (>200 %) than the -COOH oxidation type (175 %~200 %). As shown in Figure 4. 9 (b), when the CNC (110) plane interacts with GO, -OH oxidation type on GO can bring more inter-plane hydrogen bonds (~30 %) than the pristine structure. On the contrary, the total number of hydrogen bonds slightly decreases when the CNC (110) plane interacts with GO-COOH plane. Since the double bonded oxygen of -COOH functional groups in GO only serves as the acceptor, but the oxygen of -OH functional groups on GO serves as the donor and acceptor simultaneously when interacting with the CNC slab. As the oxygen densities of two types of GO are the same, there should be fewer unique D-H pairs in statistics from GO-COOH cases due to the absence of donors from double bonded oxygen side, which is consistent with what we have observed in Figure 4. 9 (a) and (b).

For all the cases shown in Figure 4. 9 (a) and (b), more D-H pairs are from CNC when interacting with GO-COOH than with the GO-OH, especially at the (200) CNC-GO interface. The CNC (200) GO-COOH has the most D-H pairs. It is because that -COOH functional groups on GO have greater polarity than -OH functional groups. On the other hand, CNC (110) plane and (200) plane by nature present the hydrophilic and the

hydrophobic characters, respectively. Therefore, the -OH groups on CNC (200) plane have the potential to be pulled out towards GO due to the hydrogen bonds at the CNC-GO interface. It supports the findings in Figure 4. 6 that more hydrogen atoms on -OH terminal groups flip in→out at the CNC (200) interface layer when interacting with GO-COOH than interacting with GO-OH. Meanwhile, for the CNC (200) surfaces, the center chain layer (L10) presents slightly higher number of D-H pairs than the origin chain layer (L1), which confirms the relative inertness of origin chains.

We further investigate the specific D-H types of all the D-H pairs from the CNC with respect to the CNC slab orientation and the GO oxidation type, as shown in Figure 4. 9 (c) and (d). For the pristine CNC (200), origin chain layer (L1) of (200) plane only has O3-H3 as D-H pairs, and center chain layer (L10) only has O6-H6 as D-H pairs. For the pristine CNC (110), O3-H3 and O6-H6 pairs coexist as D-H pairs. With the CNC-GO interaction, all possible D-H types are developed, regardless of the CNC slab orientation and the GO oxidation type. In Figure 4. 9 (c), the redistribution of the D-H pairs is quite different between the origin chain layer (L1) and the center chain layer (L10). The origin chains tend to be more stable as each chain tilts counterclockwise about the axial direction with O3-H3 and O6-H6 alternatingly getting closer to the plane where the GO is placed. Whereas, the center chains tilt clockwise about the axial direction with O2-H2 pairs more favorably forming the hydrogen bonds with GO [85][97]. The big difference of D-H pairs in O3-H3 type between (200) GO-COOH and GO-OH cases at L10 is due to the greater polarity of -COOH functional groups that lead more hydrogen atoms on O3-H3 to flip out and form hydrogen bonds. This causes the highest amount of hydrogen atoms on -OH to

flip in→out at L10 of CNC (200) GO-COOH in Figure 4. 6. In Figure 4. 9 (d), there is not much difference between L1 and L10 in all cases, since these two nearest layers are essentially identical. The O2-H2 groups are initially facing to non-polar groups in the pristine CNC (110), yet turn to be exposed to CNC-GO interface following by a large amount of O2-H2 serving as the donor. The decrease in O6-H6 (the terminal group of the hydroxymethyl group) at CNC (200) L10 and CNC (110) L1 and L10 implies the presence of new conformations "*gt*" and "*gg*", since the population of "*tg*" conformation is typically believed to facilitate the formation of inter-chain hydrogen bonds at the low temperature crystalline state [86][90].

4.4 Conclusions

We have categorized the morphological variations of the CNC-GO sandwich structures into three levels of rotations: major rotation (glucose ring twisting), intermediate rotations (dihedral angle variations) and minor rotation (terminal -CH and -OH groups flipping), and reached the following conclusions:

(1) The morphological variations of the CNC at CNC-GO interface can be evaluated by three level rotations: the major rotation as the torsion of the glucose ring about the axial direction *c*; the intermediate rotations as the relative rotation of consecutive two glucose rings and the relative rotation of the glucose ring and its side chain -CH_2-OH; and the minor rotation as the flipping motion of the hydrogen atom on the -OH/-CH groups with respect to the CNC surface orientation.

(2) The major rotation and the intermediate rotations due to the CNC-GO interface interaction are limited within the first two to three layers regardless of the GO

oxidation type. However, the minor rotation induces the impact not only on the first two to three layers near the interface, but in some occasions penetrating through the entire CNC slab, highly sensitive to the CNC slab orientation and the GO oxidation type.

(3) The CNC-GO interaction introduces a locally stable energy state at the CNC interface plane, causing the detached basins in the ψ - φ distributions as well as the "*gt*"/"*gg*" conformations in the ω' - ω distributions.

(4) When the CNC (200) surface interacts with GO-COOH, more hydrogen atoms on -OH terminal groups of CNC (200) plane are flipped towards the CNC-GO interface, losing the balance of the -OH flipping dynamics.

V. MECHANICAL PROPERTY ENHANCEMENT OF THE CNC-GO NANOCOMPOSITES

5.1 Motivation

Mechanical property is an important characterization to design and develop new composite materials. As the literature reviewed in Chapter I, numerous numerical research has been done on determining mechanical properties of pristine cellulose and GO or as they are in the aqueous solution. Depending on the fabrication process, the CNC-GO membrane might contain a broad range of weight percent of water. With the hydrophilic properties of CNC and GO in nature, water molecules are difficult to be completely removed even after prolonged drying [98]. It has been observed that different magnitude of the water contents will affect the mechanical properties of the nanocomposites. In this study, we adopt the molecular dynamics simulation to perform the uniaxial tensile tests on various CNC-GO sandwich structures with respect to the CNC slab orientation, the GO oxidation type, and the water content. The objective is to investigate the mechanical property enhancement of the CNC-GO nanocomposites with respect to the stiffness, ultimate tensile strength, and toughness.

5.2 Modeling Setups

We perform the uniaxial tensile tests on the CNC-GO sandwich structures with 10-layer CNC slabs, shown in Figure 3. 3, with and without water contents. Various CNC slab orientations and GO oxidation types are considered. The weight percentage of the water molecules varies from 3 wt.% to 16 wt.%. Uniaxial tensile tests are

performed at 100K in three orthogonal directions (Figure 5. 1 (a)) until reaching to the failure. The *z* direction represents the CNC chain direction regardless of the CNC slab orientation. The strain rate is selected to be 10^{10} /s under the NPT ensemble. The timestep size is 0.5 fs.

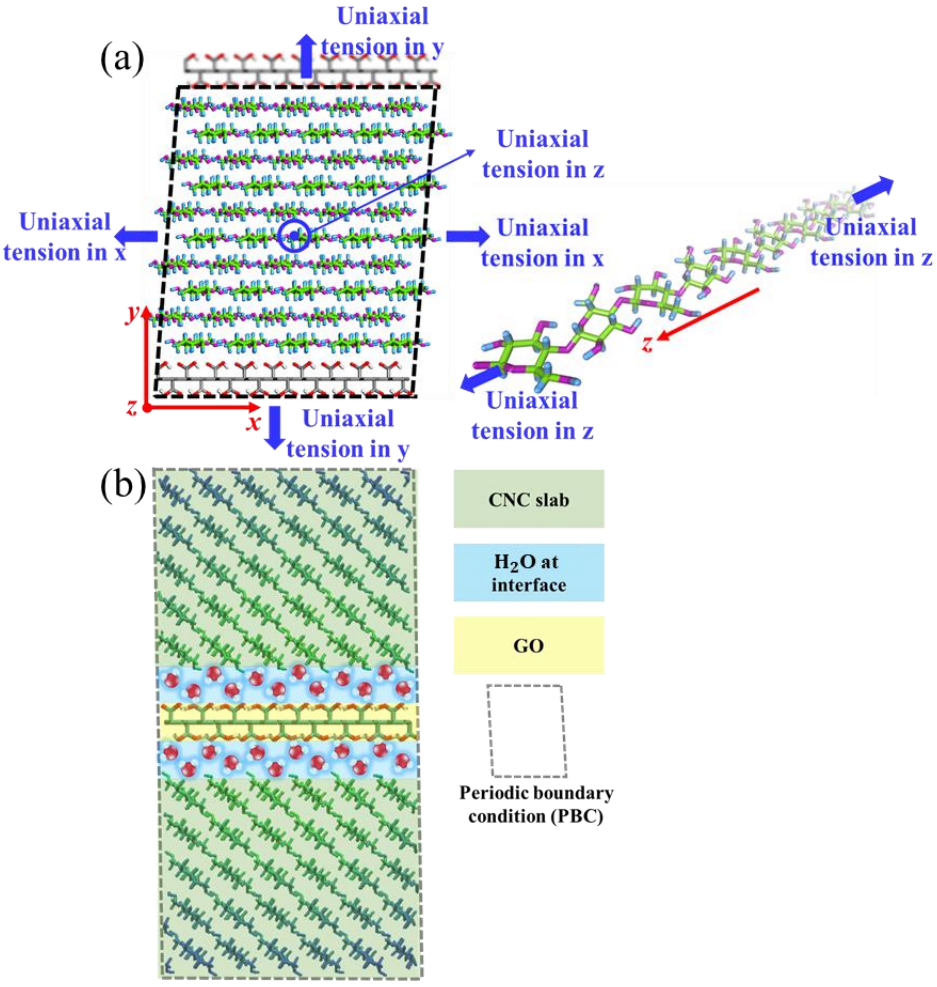

Figure 5. 1: (a) The schematic of conducting uniaxial tensile tests in x, y and z directions on a CNC-GO sandwich structure of (200) orientation with PBC imposed; (b) The schematic of CNC-GO sandwich structure of (110) orientation in the presence of interface water molecules. The grey dash borders represent the PBC for the sandwich structures. Note that in Figure 5. 1 (a), the x and z directions are in alignment with CNC-GO lattice principal directions, whereas z is parallel to the CNC fiber molecular chain direction, as shown on the right. The y direction is not parallel to any of the CNC-GO lattice principal directions due to the monoclinic structure of Iβ CNC.

5.3 Results and Discussion

5.3.1 Mechanical Properties of Pristine Cellulose

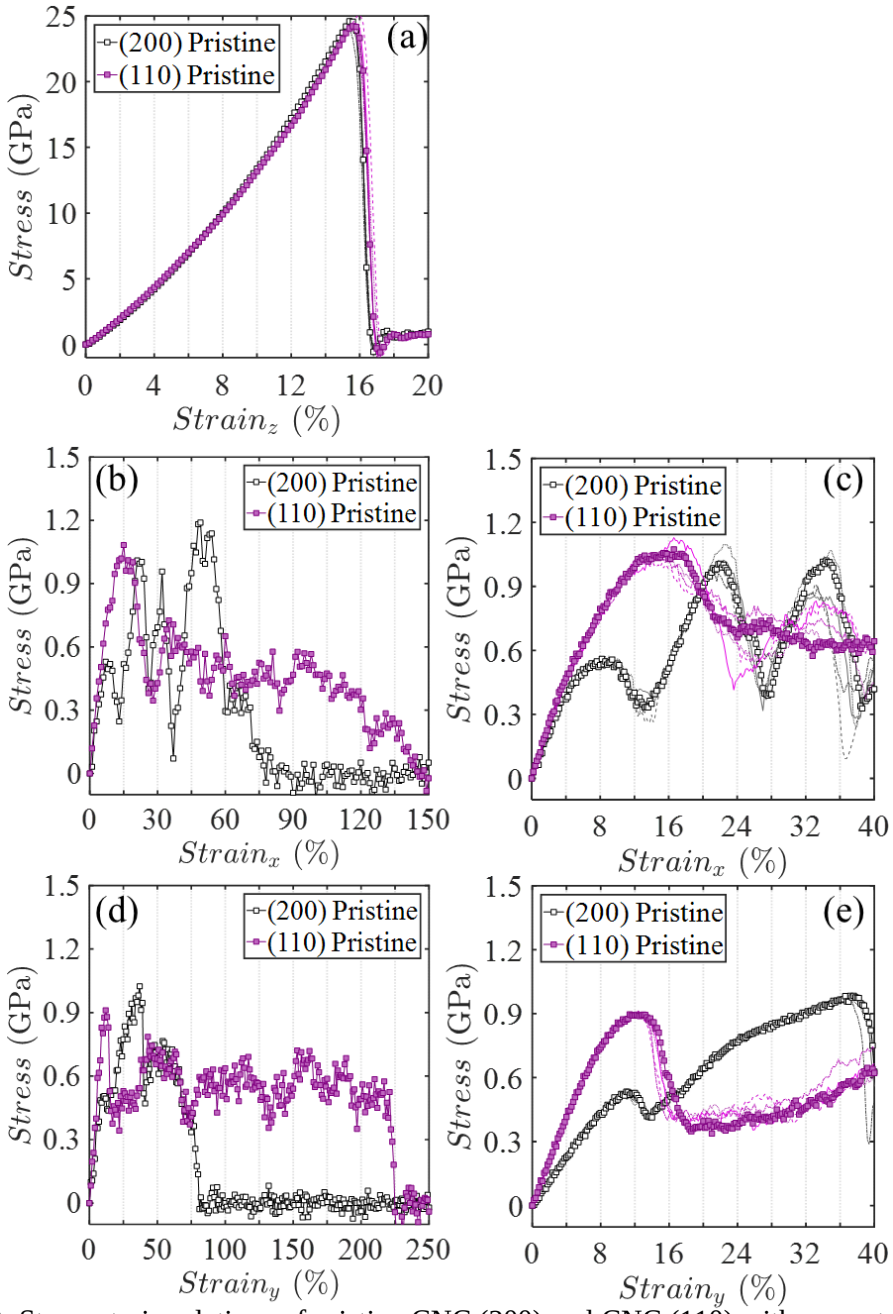

Figure 5. 2: Stress-strain relations of pristine CNC (200) and CNC (110) with respect to different loading directions. (a) Tensile loading in z direction from 0 to 20 % strain; (b) tensile loading in x direction from 0 to 150 % strain; (c) tensile loading in x direction from 0 to 40 % strain; (d) tensile loading in y direction from 0 to 250 % strain; (e) tensile loading in y direction from 0 to 40 % strain.

In Figure 5. 2, the stress-strain relations of pristine CNC (200) and CNC (110) are presented in black open square and purple solid square symbols, respectively. Multiple cases with respect to different relaxed configurations are also recorded and plotted with different line styles but identical colors in Figure 5. 2 (a), (c) and (e). When the uniaxial tensile loading is applied along the CNC fiber direction (*z*), shown in Figure 5. 2 (a), the Young's modulus and ultimate tensile strength are much larger in magnitude than those in the other two directions. With the 2nd order polynomial fitting within 4.0 % strain, the Young's moduli are evaluated to be 86.6±0.7 GPa and 89.5±0.7 GPa for pristine CNC (200) and CNC (110), respectively. When the CNC fibers break, the ultimate tensile strengths from CNC (200) and CNC (110) are about the same.

For pristine CNC (200), the Young's modulus in *x* direction is much smaller than that in *z* direction, which is closely related with the hydrogen bonding network density and distribution. In CNC (200), the tensile loading is applied in the transverse direction of the CNC fiber, where the hydrogen bonds, rather than covalent bonds, dominate the strength and ductility. The fracture happens when the hydroxyl groups between the neighboring CNC chains are pulled apart by a cutoff distance (6.0 Å in this study). Since the CNC (110) chains initially have a tilt angle with respect to the horizontal direction (*x*), it takes more strain in *x* direction than CNC (200) to firstly straighten out and then to be pulled apart. In Figure 5. 2 (c), there appear a few kinks of strain softening and hardening after yielding, which can be attributed to the plane slips along (110) and (1-10) planes over the elevated

strain in *x* direction, where the hydrogen bonds undergo breaking, rearranging and reforming.

	(200) Pristine			(110) Pristine		
Loading Direction	***x***	***y***	***z***	***x***	***y***	***z***
Young's Modulus (GPa)	11.2 ±0.4	6.2 ±0.5	86.6 ±0.7	13.4 ±0.3	10.7 ±0.2	89.5 ±1.0
	(200) GO-COOH			**(110) GO-COOH**		
Loading Direction	***x***	***y***	***z***	***x***	***y***	***z***
Young's Modulus (GPa)	104.6 ±2.6	12.3 ±0.6	147.8 ±0.9	106.6 ±1.5	16.0 ±0.4	141.5 ±2.1
	(200) GO-OH			**(110) GO-OH**		
Loading Direction	***x***	***y***	***z***	***x***	***y***	***z***
Young's Modulus (GPa)	82.3 ±1.5	12.8 ±0.5	140.1 ±1.0	77.7 ±0.8	15.5 ±0.4	126.1 ±1.1
	(200) GO-COOH + H_2O (*z*)			**(110) GO-COOH + H_2O (*z*)**		
H_2O Contents (wt. %)	**3**	**6**	**16**	**3**	**6**	**16**
Young's Modulus (GPa)	144.5 ±2.4	146.8 ±1.5	140.0 ±2.2	138.7 ±2.0	143.5 ±2.5	135.4 ±1.2

Table 5. 1: Mechanical properties of pristine CNCs, sandwich structures and those including various interface water contents.

Conducting the uniaxial tensile test in *y* direction, the CNC (200) chains turn to go upright along the loading direction. Analogous with that in response to the *x* direction tensile loading, the hydrogen bonds experience breaking, rearranging and reforming, which accommodates to the strain softening and hardening after yielding, shown in Figure 5. 2 (e). After that, the CNC (200) lattice structure becomes disordered, and then continues being stretched until the fracture point. Unlike the alternating spatial arrangement of the origin and center chain layers of CNC (200), the stacking pattern of CNC (110) gives rise

to a more uniform hydrogen bonding network distribution over the elevated strain in *y* direction.

As listed in Table 5. 1, the Young's moduli along CNC fiber longitudinal (*z*) direction for (200) orientation and (110) orientation are 86.6±0.7 GPa and 89.5±1.0 GPa, which are consistent with the experimental measurements 58~180 GPa for cellulose crystals [99][100][101][102][103][104][105][106]. The transverse moduli of *x* and *y* directions are 11.2±0.4 GPa and 6.2±0.5 GPa for CNC (200), and 13.4±0.3 GPa and 10.7±0.2 GPa for CNC (110), respectively. These also fall in the range of reported values 2~50 GPa from experimental measurements [107][108][109][110].

5.3.2 Mechanical Properties of Graphene Oxide

Monolayer GO has been found to have lower Young's modulus and ultimate tensile strength than unfunctionalized carbon-based nanomaterials, such as pristine graphene and carbon nanotubes [111][112][113][114]. In addition, it has been reported that the Young's

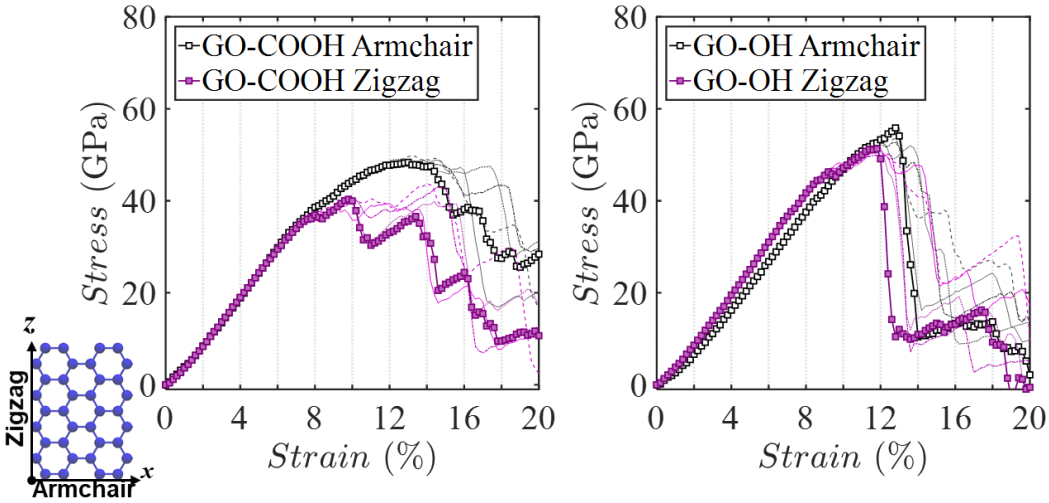

Figure 5. 3: Stress-strain behaviors of GOs under tensile loading in *x* (armchair direction, black open square symbols) and *z* (zigzag direction, purple solid square symbols) directions: (a) GO with -COOH oxidation; (b) GO with -OH oxidation.

modulus and strength monotonically decrease as the oxidation ratio increases [111][115]. The stress-strain relations of GO-COOH and GO-OH are shown in Figure 5. 3 (a) and (b), respectively. Multiple cases with respect to different relaxed configurations are included. The Young's moduli of GO-COOH in the armchair and zigzag directions are 360.5±7.4 GPa and 389.4±19.2 GPa, and those of GO-OH in the armchair and zigzag directions are 259.3±6.0 GPa and 385.8±19.2 GPa. We also have tested different initial orientations of -OH groups on GO at 44 % oxidation ratio, the Young's modulus of GO-OH is always smaller than that of GO-COOH under armchair loading. The above Young's moduli of GO fall into the experimentally measured range 200 GPa~500 GPa [116][117], and the trend of lower Young's modulus of armchair direction than zigzag direction is also identified by various MD work as the oxidation ratio around 40 % [115][118][119].

5.3.3 Mechanical Properties of CNC-GO Sandwich Structures

The stress-strain relations of 10-layer CNC-GO sandwich structures are plotted in Figure 5. 4 with respect to various CNC slab orientations and GO oxidation types under the tensile loading in *z*, *x* and *y* directions, respectively. Multiple cases of sandwich structures with respect to different relaxed configurations are included.

Figure 5. 4 (a) and (b) represent the stress-strain relation of CNC-GO sandwich structures as the tensile loading is applied along the CNC fiber direction (*z* direction). As listed in Table 5. 1, the Young's modulus of a CNC-GO sandwich structure is much larger than that of the pristine CNC, regardless of the CNC slab orientation and the GO oxidation

type. Before reaching to the ultimate tensile strength, one or two kinks can be observed in the strain-stress relations, regardless of the CNC slab orientation and the GO oxidation type.

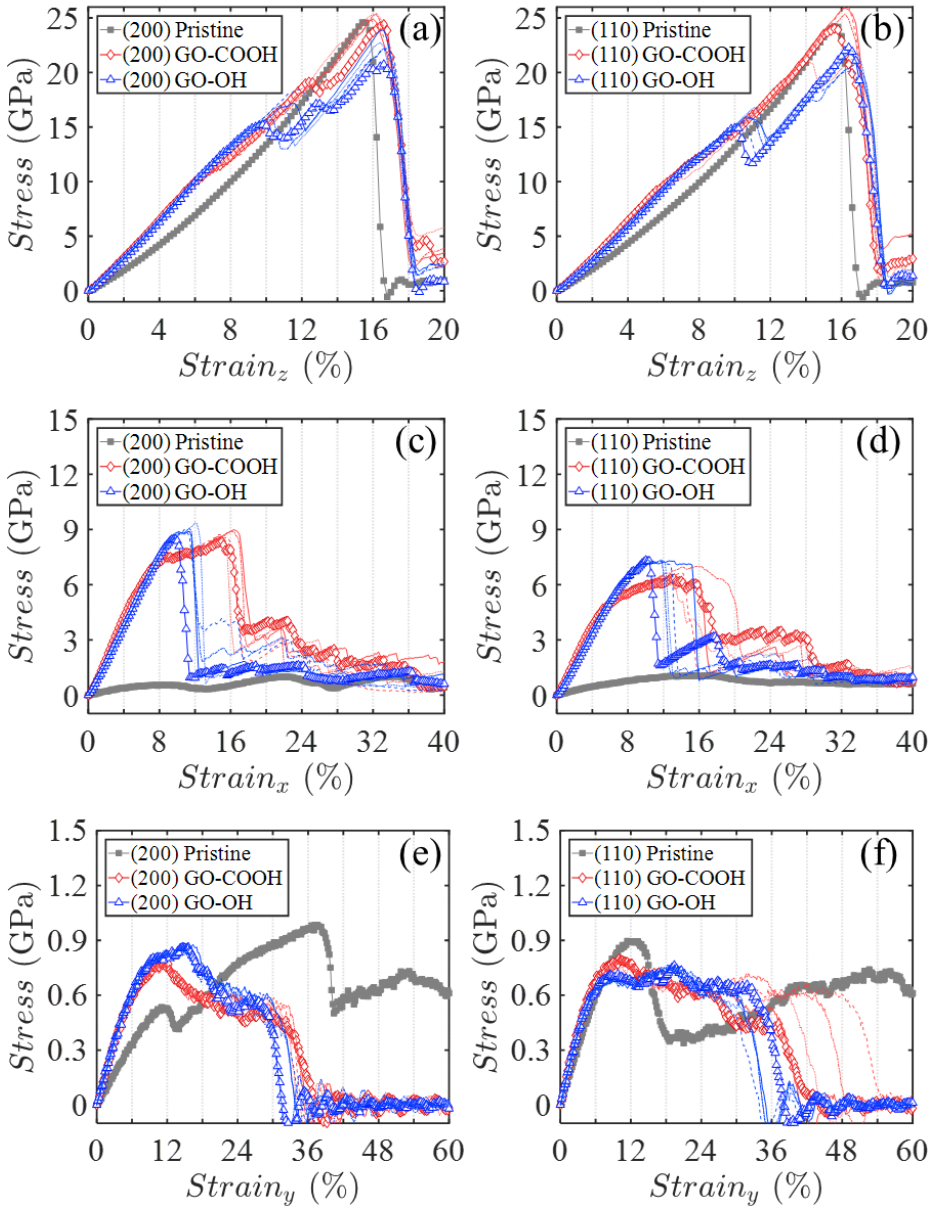

Figure 5. 4: Stress-strain behaviors of CNC-GO sandwich structures with respect to various CNC slab orientations and GO oxidations: (a) (200) orientation and tensile loading in z direction; (b) (110) orientation and tensile loading in z direction; (c) (200) orientation and tensile loading in x direction; (d) (110) orientation and tensile loading in x direction; (e) (200) orientation and tensile loading in y direction; (f) (110) orientation and tensile loading in y direction.

The failure of the GO causes the stress redistribution and forms the first kink before the entire sandwich structure fails. Particularly, the second kink of CNC (200) GO-OH sandwich structure that randomly occurs is attributed to the single cellulose chain breakage adjacent to the GO.

As shown in Figure 5. 4 (c) and (d), the presence of GO in the nanocomposite substantially enhances the stiffness, ultimate tensile strength and toughness of the CNC-GO structures along *x* direction, regardless of the CNC orientation and the GO oxidation type. The GO-COOH sandwich structures have higher Young's moduli than GO-OH sandwich structures due to the significantly higher stiffness of GO-COOH than GO-OH in *x* (armchair) direction, as identified in Figure 5. 3. As can be observed, GO reaches to the failure earlier than CNC slabs during the tensile loading along *x* direction.

Figure 5. 4 (e) and (f) show the stress-strain behaviors of sandwich structures in response to *y* direction tensile loading. Since the loading direction is along the out-of-plane direction of GO, the mechanical properties are not significantly improved, compared to the other two directions. The hydrogen bonding networks at the CNC-GO interfaces plays an important role in improving the Young's modulus of sandwich structures of (200) orientation. The failure is followed by the detachment of CNC planes along *y* direction.

5.3.4 Mechanical Properties of Sandwich Structures with Interface Water

The presence of interface water molecules can change the hydrogen bonding networks at the interface, therefore affect the mechanical properties of the nanocomposites. We perform the uniaxial tensile tests along *z* direction at the strain rate of 10^{10} /s with respect to the CNC/10 (200) GO-COOH and CNC/10 (110) GO-COOH structures at

various water contents: 0 wt.%, 3 wt.%, 6 wt.% and 16 wt.%. The stress-strain relations are presented in Figure 5. 5 (a)~(d).

Under such a high strain rate (10^{10} /s), the effects of existing water contents on the mechanical properties of the CNC-GO sandwich structures are very limited. The Young's modulus variations are limited within 6 %, regardless of the CNC orientation. However, the existence of interface water molecules can greatly modify the hydrogen bonding

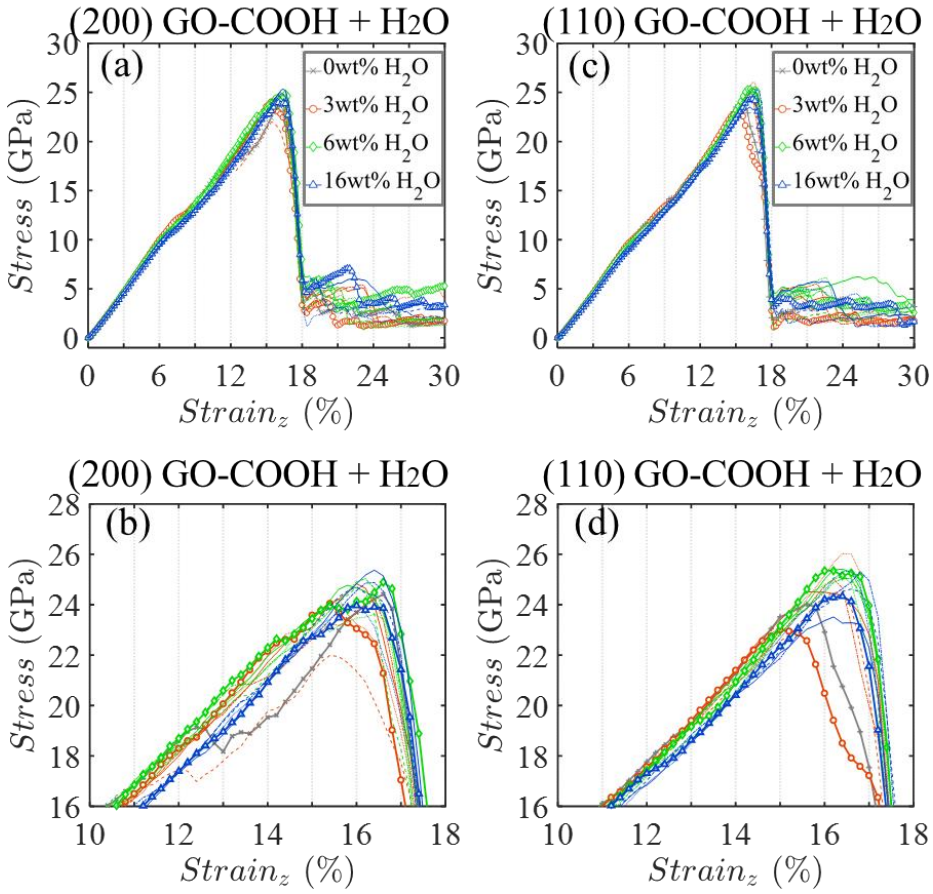

Figure 5. 5: Stress-strain behaviors of the CNC-GO sandwich structures in the presence of interface water molecules at 0 wt.%, 3 wt.%, 6 wt.% and 16 wt.% contents as the tensile loading is applied in *z* direction. (a) Stress-strain relation of (200) GO-COOH interface; (b) zoomed-in stress-strain relation of (200) GO-COOH interface; (c) stress-strain relation of (110) GO-COOH interface; (d) zoomed-in stress-strain relation of (110) GO-COOH interface.

networks within the CNC-GO structures, therefore affecting the failure behaviors of the CNC-GO structures. Compared to the sandwich structures with no interface water molecules, the sandwich structures in the presence of 6 wt.% and 16 wt. % interface water contents typically do not exhibit obvious kinks before the failure points, rather, the stress-strain curves are smoother. Taking the sandwich structure of CNC/10 (200) GO-COOH with 6 wt.% interface water content as an example, the GO first undergoes fracture at ~9 % strain, yet the entire structure fails at ~17 % strain. Right after that, CNC chains at the interface break, shown in Figure 5. 6.

In order to identify distinct mechanical behaviors of sandwich structures with various water contents, we count the percentage of hydrogen bond changes relative to those

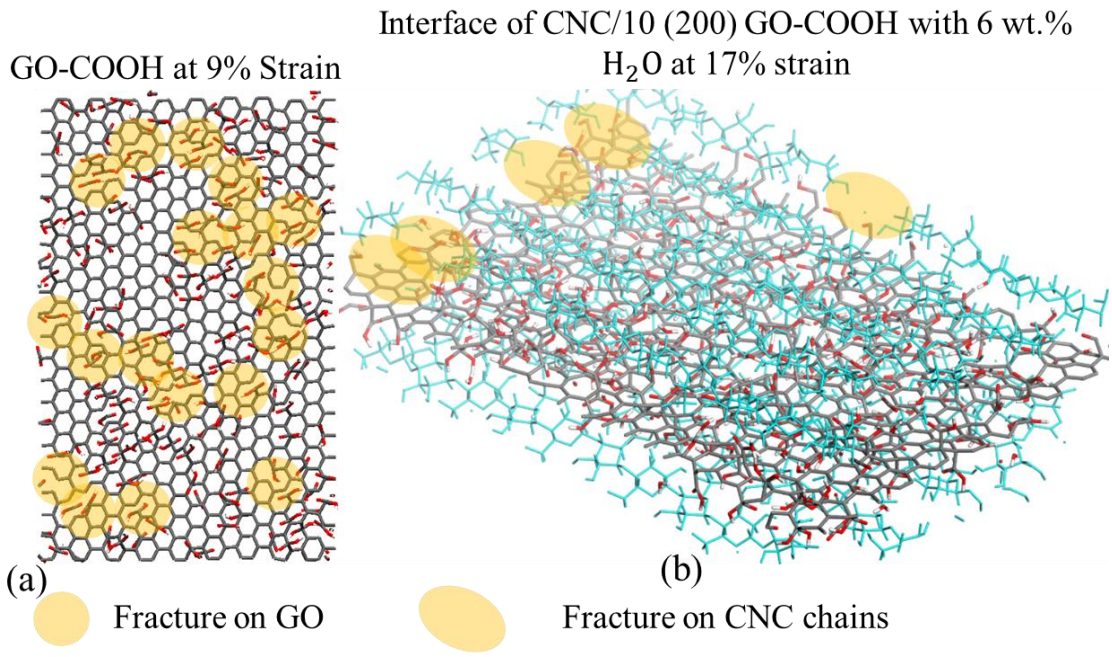

Figure 5. 6: The schematics of failures on GO and on CNC chains at the interface of CNC/10 (200) GO-COOH with 6 wt.% H_2O. (a) Failure occurs on GO-COOH at 9 % strain; (b) failure subsequently occurs on CNC chains at 17 % strain and the entire structure fails. The yellow round and elliptical shaded areas represent the fracture points on GO and CNC chains, respectively.

of the relaxed configurations, within the interface as described in Figure 5. 6 (b). The interface we inspect contains two nearest 1st CNC layers above and below the GO, and the water molecules of various contents between each CNC and GO.

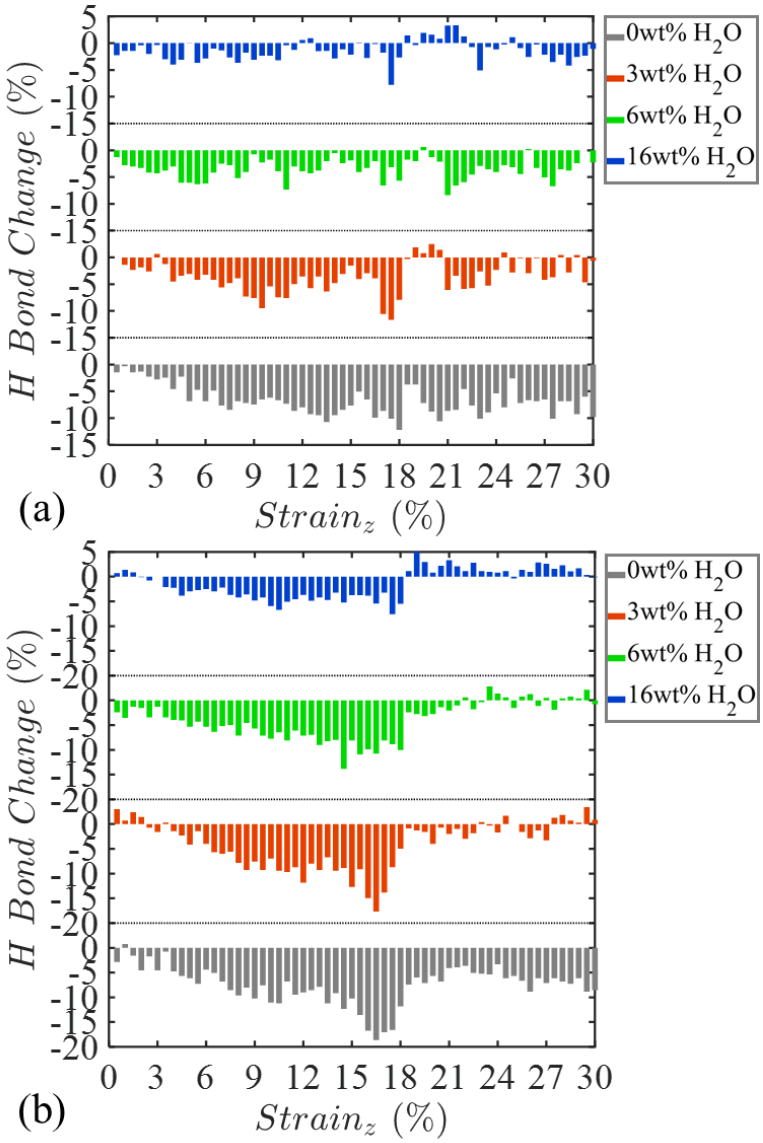

Figure 5. 7: The percentage of hydrogen bond number changes relative to the relaxed states for the GO-COOH type sandwich structures in the presence of interface water molecules at 0 wt.%, 3 wt.%, 6 wt.% and 16 wt.% contents as the tensile loading is applied in z direction. All hydrogen bond counts are based on the CNC$-H_2O-$GO$-H_2O-$CNC interface as shown in Figure 5. 6 (b). (a) The interface of (200) orientation; (b) the interface of (110) orientation. The negative and positive percentages represent the reduction and increase in hydrogen bonds over the elevated strain.

Figure 5. 7 (a) and (b) report the hydrogen bond number changes in percentage over the elevated strain for GO-COOH sandwich structures with water contents to be 0 wt.%~16 wt.% of (200) and (110) orientations, respectively. The negative and positive counts in percentage represent the reduction and increase in hydrogen bonds during the tensile tests. With the increasing water contents, there is less hydrogen bond reduction in percentage before the failure point. The sharp hydrogen bond reductions between 15 % and 18 % strain in CNC-GO sandwich structures of 0 wt.% and 3 wt.% interface water contents represent their failure points of the entire structures, regardless of the CNC orientation. And the small hydrogen bond reductions around 9 % strain for these two water contents correspond to the GO failure, as pointed out earlier. In Figure 5. 7 (b), for 6 wt.% and 16 wt.% interface water structures, the hydrogen bond reductions at around failure points are rather gentle, which implicate better ductility.

5.4 Conclusion

We adopt the molecular dynamics simulation to perform the uniaxial tensile tests of the various CNC-GO sandwich structures with respect to the CNC slab orientations, GO oxidation types, and water contents. The conclusions are listed as follows.

(1) The embedment of GO significantly enhances the stiffness of the composite in response to the tensile loadings along the in-plane directions of the GO, regardless of the CNC slab orientation and the GO oxidation type.

(2) With the strain rate of 10^{10} /s, the effect of the water contents on the stiffness of CNC-GO structures can be neglected. The modified hydrogen bonding

networks due to the existence of the interface water molecules will slightly affect the ultimate tensile strength of the CNC-GO structures.

VI. CONCLUSIONS

In this research, we adopt the ReaxFF force field into the classical molecular dynamics simulation to systematically investigate the CNC-GO interface interaction based on Iβ CNC-GO sandwich structures with respect to various CNC slab orientations, CNC slab thicknesses, GO oxidation types, and water contents at the interface. The objective of this research is to understand the role of hydrogen bonding networks in the XRD spectrum variations, CNC morphological variations and mechanical property enhancement of the CNC-GO nanocomposites. The conclusions are listed below:

(1) The hydrogen bonds at the CNC-GO interface induce a non-uniform strain field to the CNC structure, including a global strain throughout the CNC slab and a local strain near the CNC-GO interface.

(2) The interaction at (200) CNC-GO interface largely causes the broadening and weakening of the (200) peak. The interaction at (110) CNC-GO interface enhances the intensity of (1-10)/(110) peaks since the two peaks tend to shift closer to each other with decreasing CNC slab thicknesses.

(3) The morphological variations of the CNC at CNC-GO interface can be evaluated by three level rotations: the major rotation as the torsion of the glucose ring about the axial direction *c*; the intermediate rotations as the relative rotation of consecutive two glucose rings and the relative rotation of the glucose ring and its side chain -CH_2-OH; and the minor rotation as the flipping motion

of the hydrogen atom on the -OH/-CH groups with respect to the CNC surface orientation.

(4) The major rotation and the intermediate rotations due to the CNC-GO interface interaction are limited within the first two to three layers regardless of the GO oxidation type. However, the minor rotation induces the impact not only on the first two to three layers near the interface, but in some occasions penetrating through the entire CNC slab, highly sensitive to the CNC slab orientation and the GO oxidation type.

(5) When the CNC (200) surface interacts with GO-COOH, more hydrogen atoms on -OH terminal groups of CNC (200) plane are flipped towards the CNC-GO interface, losing the balance of the -OH flipping dynamics.

(6) The embedment of GO significantly enhances the stiffness of the composite in response to the tensile loadings along the in-plane directions of the GO, regardless of the CNC slab orientation and the GO oxidation type.

(7) With the strain rate of 10^{10} /s, the effect of the water contents on the stiffness of CNC-GO structures can be neglected. The modified hydrogen bonding networks due to the existence of the interface water molecules will slightly affect the ultimate tensile strength of the CNC-GO structures.

REFERENCES

[1] C. Somerville, “Cellulose synthesis in higher plants”, Annu. Rev. Cell Dev. Biol., **22**, 53-78, 2006.

[2] A. T. Olek, C. Rayon, L. Makowski, H. R. Kim, P. Ciesielski, J. Badger, L. N. Paul, S. Ghosh, D. Kihara, M. Crowley, and M. E. Himmel, 2014. “The structure of the catalytic domain of a plant cellulose synthase and its assembly into dimers”, The Plant Cell, **26**(7), 2996-3009, 2014.

[3] M. Poletto, V. Pistor, and A. J. Zattera, “Structural characteristics and thermal properties of native cellulose”, Cellulose-fundamental aspects, Ed. Van de Ven, T. and Gdbout, L. InTech, 45-68, 2013.

[4] A. P. Heiner, J. Sugiyama, and O. Teleman, “Crystalline cellulose Iα and Iβ studied by molecular dynamics simulation”, Carbohydrate Research, **273**(2), 207-223, 1995.

[5] C. M. Lee, N. M. Mohamed, H. D. Watts, J. D. Kubicki, and S. H. Kim, “Sum-frequency-generation vibration spectroscopy and density functional theory calculations with dispersion corrections (DFT-D2) for cellulose Iα and Iβ”, The Journal of Physical Chemistry B, **117**(22), 6681-6692, 2013.

[6] M. Genet, A. Stokes, F. Salin, S. B. Mickovski, T. Fourcaud, J. F. Dumail and R. Van Beek, “The influence of cellulose content on tensile strength in tree roots”, Plant and soil, **278**(1), 1-9, 2005.

[7] Y. Habibi, L. A. Lucia, and O. J. Rojas, “Cellulose nanocrystals: chemistry, self-assembly, and applications”, Chemical Reviews, **110**, 3479-3500, 2010.

[8] Q. Mao, L. Yang, X. Geng, L. Chen, B. Sapkota, H. Zhao, and H. Zhu, “Interface Strain Induced Hydrophobic Facet Suppression in Cellulose Nanocomposite Embedded with Highly Oxidized Monolayer Graphene Oxide”, Advanced Materials Interfaces, 1700995, 2017.

[9] A. Lerf, H. He, M. Forster, and J. Klinowski, “Structure of graphite oxide revisited”, The Journal of Physical Chemistry B, **102**(23), 4477-4482, 1998.

[10] D. R. Dreyer, S. Park, C. W. Bielawski & R. S. Ruoff, “The chemistry of graphene oxide”, Chemical Society Reviews, **39**(1), 228-240, 2010.

[11] L. Valentini, M. Cardinali, E. Fortunati, L. Torre, and J. M. Kenny, “A novel method to prepare conductive nanocrystalline cellulose/graphene oxide composite films”, Materials Letters, **105**, 4-7, 2013.

[12] K. K. Sadasivuni, A. Kafy, L. Zhai, H. U. Ko, S. Mun, & J. Kim, “Transparent and flexible cellulose nanocrystal/reduced graphene oxide film for proximity sensing”, Small, 11(8), 994-1002, 2015.

[13] R. Xiong, K. Hu, A. M. Grant, R. Ma, W. Xu, C. Lu & V. V. Tsukruk, “Ultrarobust transparent cellulose nanocrystal-graphene membranes with high electrical conductivity”, Advanced Materials, **28**(7), 1501-1509, 2016.

[14] Y. Wen, M. Wu, M. Zhang, C. Li & G. Shi, “Topological design of ultrastrong and highly conductive graphene films”, Advanced Materials, 2017.

[15] N. D. Luong, N. Pahimanolis, U. Hippi, J. T. Korhonen, J. Ruokolainen, L. S. Johansson, J. D. Nam, and J. Seppälä, “Graphene/cellulose nanocomposite paper with high electrical and mechanical performances”, Journal of Materials Chemistry, **21**(36), 13991-13998, 2011.

[16] R. Alqus, S. J. Eichhorn & R. A. Bryce, “Molecular dynamics of cellulose amphiphilicity at the graphene-water interface”, Biomacromolecules, **16**(6), 1771-1783, 2015.

[17] S. Montes, P. M. Carrasco, V. Ruiz, G. Cabañero, H. J. Grande, J. Labidi & I. Odriozola, “Synergistic reinforcement of poly (vinyl alcohol) nanocomposites with cellulose nanocrystal-stabilized graphene”, Composites Science and Technology, **117**, 26-31, 2015.

[18] R. Kabiri & H. Namazi, “Nanocrystalline cellulose acetate (NCCA)/graphene oxide (GO) nanocomposites with enhanced mechanical properties and barrier against water vapor”, Cellulose, **21**(5), 3527-3539, 2014.

[19] L. Valentini, M. Cardinali, E. Fortunati & J. M. Kenny, “Nonvolatile memory behavior of nanocrystalline cellulose/graphene oxide composite films”, Applied Physics Letters, **105**(15), 153111, 2014.

[20] N. D. Luong, N. Pahimanolis, U. Hippi, J. T. Korhonen, J. Ruokolainen, L. S. Johansson, J. D. Nam, and J. Seppälä, “Graphene/cellulose nanocomposite paper with high electrical and mechanical performances”, Journal of Materials Chemistry, **21**(36), 13991-13998, 2011.

[21] Q. Zheng, Z. Cai, Z. Ma, and S. Gong, "Cellulose nanofibril/reduced graphene oxide/carbon nanotube hybrid aerogels for highly flexible and all-solid-state supercapacitors", ACS Applied Materials & Interfaces, **7**(5), 3263-3271, 2015.

[22] V. L. Pushparaj, M. M. Shaijumon, A. Kumar, A. Murugesan, L. Ci, R. Vajtai, R. J. Linhardt, O. Nalamasu, and P. M. Ajayan, P.M., "Flexible energy storage devices based on nanocomposite paper", Proceedings of the National Academy of Sciences, **104**(34), 13574-13577, 2007.

[23] M. Nogi, and H. Yano, "Transparent nanocomposites based on cellulose produced by bacteria offer potential innovation in the electronics device industry", Advanced Materials, **20**(10), 1849-1852, 2008.

[24] A. Samir, M. A. S., F. Alloin, and A. Dufresne, "Review of recent research into cellulosic whiskers, their properties and application in nanocomposite field", Biomacromolecules, **6**(2), 612-626, 2005.

[25] N. Lavoine, L. Desloges, A. Dufresne and J. Bras, "Microfibrillated cellulose-Its barrier properties and applications in cellulosic materials: A review", Carbohydrate polymers, **90**(2), 735-764, 2012.

[26] F. L. Dri, L. G. Hector, R. J. Moon, and P. D. Zavattieri, "Anisotropy of the elastic properties of crystalline cellulose Iβ from first principles density functional theory with Van der Waals interactions", Cellulose, **20**(6), 2703-2718, 2013.

[27] R. J. Moon, A. Martini, J. Nairn, J. Simonsen and J. Youngblood, "Cellulose nanomaterials review: structure, properties and nanocomposites", Chemical Society Reviews, **40**(7), 3941-3994, 2011.

[28] S. Besombes and K. Mazeau, “The cellulose/lignin assembly assessed by molecular modeling. Part 2: seeking for evidence of organization of lignin molecules at the interface with cellulose”, Plant Physiology and Biochemistry, **43**(3), 277-286, 2005.

[29] Y. Nishiyama, P. Langan, and H. Chanzy, “Crystal structure and hydrogen-bonding system in cellulose Iβ from synchrotron X-ray and neutron fiber diffraction”, Journal of the American Chemical Society, **124**(31), 9074-9082, 2002.

[30] Y. Li, H. Zhu, S. Zhu, J. Wan, Z. Liu, O. Vaaland and L. Hu, “Hybridizing wood cellulose and graphene oxide toward high-performance fibers”, Npg Asia Materials, 7(1), e150, 2015.

[31] Y. Maréchal and H. Chanzy, “The hydrogen bond network in Iβ cellulose as observed by infrared spectrometry”, Journal of molecular structure, **523**(1), 183-196, 2000.

[32] X. Zhang, M. A. Tschopp, M. F. Horstemeyer, S. Q. Shi, and J. Cao, “Mechanical properties of amorphous cellulose using molecular dynamics simulations with a reactive force field”, International Journal of Modelling, Identification and Control, **18**(3), 211-217, 2013.

[33] J. A. Diaz, X. Wu, A. Martini, J. P. Youngblood, and R. J. Moon, “Thermal expansion of self-organized and shear-oriented cellulose nanocrystal films”, Biomacromolecules, **14**(8), 2900-2908, 2013.

[34] K. Chenoweth, A. C. Van Duin, and W. A. Goddard, “ReaxFF reactive force field for molecular dynamics simulations of hydrocarbon oxidation”, The Journal of Physical Chemistry A, **112**(5), 1040-1053, 2008.

[35] F. L. Dri, X. Wu, R. J. Moon, A. Martini and P. D. Zavattieri, “Evaluation of reactive force fields for prediction of the thermo-mechanical properties of cellulose Iβ”, Computational Materials Science, **109**, 330-340, 2015.

[36] A. C. Van Duin, S. Dasgupta, F. Lorant, and W. A. Goddard, “ReaxFF: a reactive force field for hydrocarbons”, The Journal of Physical Chemistry A, **105**, 9396-9409, 2001.

[37] N. V. Medhekar, A. Ramasubramaniam, R. S. Ruoff and V. B. Shenoy, “Hydrogen bond networks in graphene oxide composite paper: structure and mechanical properties”, ACS Nano, **4**(4), 2300-2306, 2010.

[38] H. Zhu, S. Zhu, Z. Jia, S. Parviniana, Y. Li, O. Vaaland, L. Hu and T. Li, “Anomalous scaling law of strength and toughness of cellulose nanopaper”, Proceedings of the National Academy of Sciences, **112**(29), 8971-8976, 2015.

[39] S. Plimpton, P. Crozier, and A. Thompson, “LAMMPS-large-scale atomic/molecular massively parallel simulator”, Sandia National Laboratories, **18**, 2007.

[40] J. G. Lee, Computational materials science: an introduction, CRC press, 2016.

[41] V. C. Epa, D. A. Winkler, L. Tran, B. Fadeel, A. Pietroiusti ans A. A. Shvedova, Computational Approaches, Academic Press: London, 85-96, 2012.

[42] P. H. Hünenberger, “Thermostat algorithms for molecular dynamics simulations” Advanced Computer Simulation, 130-130, 2005.

[43] D. Möller and J. Fischer, “Vapor liquid equilibrium of a pure fluid from test particle method in combination with NPT molecular dynamics simulations”, Molecular Physics, **69**(3), 463-473, 1990.

[44] S. A. Adelman and J. D. Doll, “Generalized Langevin equation approach for atom/solid‐surface scattering: General formulation for classical scattering off harmonic solids”, The Journal of chemical physics, **64**(6), 2375-2388, 1976.

[45] D. Li, “The Andersen thermostat in molecular dynamics”, Communications on Pure and Applied Mathematics, **61**(1), 96-136, 2008.

[46] H. J. Berendsen, J. V. Postma, W. F. Gunsteren, A. R. H. J. DiNola and J. R. Haak, “Molecular dynamics with coupling to an external bath”, The Journal of chemical physics, **81**(8), 3684-3690, 1984.

[47] M. Parrinello and A. Rahman, “Polymorphic transitions in single crystals: A new molecular dynamics method”, Journal of Applied physics, **52**(12), 7182-7190, 1981.

[48] G. J. Martyna, D. J. Tobias and M. L. Klein, “Constant pressure molecular dynamics algorithms”, The Journal of Chemical Physics, **101**(5), 4177-4189, 2994.

[49] R. A. Lippert, C. Predescu, D. J. Ierardi, K. M. Mackenzie, M. P. Eastwood, R. O. Dror and D. E. Shaw, “Accurate and efficient integration for molecular dynamics simulations at constant temperature and pressure”, The Journal of chemical physics, **139**(16), 10B621_1, 2013.

[50] H. C. Andersen, “Molecular dynamics simulations at constant pressure and/or temperature”, The Journal of chemical physics, **72**(4), 2384-2393, 1980.

[51] W. G. Hoover, “Constant-pressure equations of motion” Physical Review A, **34**(3), 2499, 1986.

[52] G. J. Martyna, D. J. Tobias and M. L. Klein, “Constant pressure molecular dynamics algorithms”, The Journal of Chemical Physics, **101**(5), 4177-4189, 1994.

[53] M. A. González, “Force fields and molecular dynamics simulations”, École thématique de la Société Française de la Neutronique, **12**, 169-200, 2011.

[54] D. Jefferies and S. Khalid, “Molecular Simulations of Complex Membrane Models”, Modeling of Microscale Transport in Biological Processes, 1-18, 2017.

[55] G. Siqueira, J. Bras, A. Dufresne, “Cellulose whiskers versus microfibrils: influence of the nature of the nanoparticle and its surface functionalization on the thermal and mechanical properties of nanocomposites”, Biomacromolecules, **10**, 425-432, 2008.

[56] C. Bonini, L. Heux, J. Y. Cavaillé, P. Lindner, C. Dewhurst, P. Terech, “Rodlike cellulose whiskers coated with surfactant: a small-angle neutron scattering characterization”, Langmuir, **18**, 3311-3314, 2002.

[57] P. Tingaut, T. Zimmermann, F. Lopez-Suevos, “Synthesis and characterization of bionanocomposites with tunable properties from poly (lactic acid) and acetylated microfibrillated cellulose”, Biomacromolecules, **11**, 454-464, 2009.

[58] S. Besombes and K. Mazeau, “The cellulose/lignin assembly assessed by molecular modeling. Part 2: seeking for evidence of organization of lignin molecules at the interface with cellulose”, Plant Physiology and Biochemistry, **43**(3), 277-286, 2005.

[59] M. Wada, L. Heux, J. Sugiyama, “Polymorphism of Cellulose I Family: Reinvestigation of Cellulose I VI” Biomacromolecules, **5**, 1385-1391, 2004.

[60] L. Segal, J. J. Creely, A. E. Martin, C. M. Conrad, “An Empirical Method for Estimating the Degree of Crystallinity of Native Cellulose Using the X-Ray Diffractometer”, Textile Research Journal, **29**, 786-794, 1959.

[61] A. N. Fernandes, L. H. Thomas, C. M. Altaner, P. Callow, V. T. Forsyth, D. C. Apperley, C. J. Kennedy and M. C. Jarvis, “Nanostructure of cellulose microfibrils in spruce wood”, Proceedings of the National Academy of Sciences, **108**(47), E1195-E1203, 2011.

[62] T. C. Gomes, and M. S. Skaf, “Cellulose-Builder: A toolkit for building crystalline structures of cellulose”, Journal of computational chemistry, **33**(14), 1338-1346, 2012.

[63] B. P. Brooks, R. E. Bruccoleri, B. D. Olafson, D. J. States, S. A. Swaminathan and M. Karplus, “CHARMM: a program for macromolecular energy, minimization, and dynamics calculations”, Journal of computational chemistry, **4**(2), 187-217, 1983.

[64] P. K. Weiner and P. A. Kollman, “AMBER: Assisted model building with energy refinement: A general program for modeling molecules and their interactions”, Journal of Computational Chemistry, **2**(3), 287-303, 1981.

[65] H. Sun, “COMPASS: an ab initio force-field optimized for condensed-phase applications overview with details on alkane and benzene compounds”, The Journal of Physical Chemistry B, **102**(38), 7338-7364, 1998.

[66] A. K. Rappé, C. J. Casewit, K. S. Colwell, W. A. Goddard Iii, and W. M. Skiff, “UFF, a full periodic table force field for molecular mechanics and molecular

dynamics simulations", Journal of the American Chemical Society, **114**(25), 10024-10035, 1992.

[67] S. L. Mayo, B. D. Olafson, and W. A. Goddard, "DREIDING: a generic force field for molecular simulations", Journal of Physical Chemistry, **94**(26), 8897-8909, 1990.

[68] P. Dauber-Osguthorpe, V. A. Roberts, D. J. Osguthorte, J. Wolff, M. Genest, and A. T. Hagler, Proteins: Structure, Function and Genetics, **4**, 31, 1988.

[69] W. R. Scott, P. H. Hünenberger, I. G. Tironi, A. E. Mark, S. R. Billeter, J. Fennen & van W. F. Gunsteren, "The GROMOS biomolecular simulation program package", The Journal of Physical Chemistry A, **103**(19), 3596-3607, 1999.

[70] L. M. Surhone, M. T. Timpledon and S. F. Marseken, Visual Molecular Dynamics, 2010.

[71] T. P. Senftle, S. Hong, M. M. Islam, S. B. Kylasa, Y. Zheng, Y. K. Shin and T. Verstraelen. "The ReaxFF reactive force field: development, applications and future directions" npj Computational Materials, **2**, 15011, 2016.

[72] X. Wu, R. J. Moon, and A. Martini, "Crystalline cellulose elastic modulus predicted by atomistic models of uniform deformation and nanoscale indentation", Cellulose, **20**, 43-55, 2013.

[73] G. R. Desiraju, "The C-H···O hydrogen bond: structural implications and supramolecular design", Accounts of Chemical Research, **29**, 441-449,1996.

[74] T. R. Mattsson, J.M.D. Lane, K.R. Cochrane, M.P. Desjarlais, A.P. Thompson, F. Pierce and G.S. Grest, “First-principles and classical molecular dynamics simulation of shocked polymers”, Physical Review B, **81**(5), 054103, 2010.

[75] O. Rahaman, A.C.T. Van Duin, W.A. Goddard and D.J. Doren, “Development of a ReaxFF reactive force field for glycine and application to solvent effect and tautomerization”, The Journal of Physical Chemistry B, **115**(2), 249-261, 2011.

[76] K. N. Kirschner, A.B. Yongye, S.M. Tschampel, J. González-Outeiriño, C.R. Daniels, B.L. Foley and R.J. Woods, “GLYCAM06: a generalizable biomolecular force field”, Carbohydrates. Journal of computational chemistry, **29**(4), 622-655, 2008.

[77] A. Paajanen and J. Vaari, “High-temperature decomposition of the cellulose molecule: a stochastic molecular dynamics study”, Cellulose, 1-13, 2017.

[78] P. Zugenmaier, "Crystalline Cellulose and Derivatives: Characterization and Structures", Springer Berlin Heidelberg, 101-174, 2008.

[79] B. Delley, “An all electron numerical method for solving the local density functional for polyatomic molecules”, The Journal of chemical physics, **92**(1), 508-517, 1990.

[80] G. Nemethy, M. S. Pottle, and H. A. Scheraga, “Energy parameters in polypeptides. 9. Updating of geometrical parameters, nonbonded interactions, and hydrogen bond interactions for the naturally occurring amino acids”, The Journal of Physical Chemistry, **87**(11), 1883-1887, 1983.

[81] R. Rahman, J. T. Foster and A. Haque, “Molecular dynamics simulation and characterization of graphene–cellulose nanocomposites”, The Journal of Physical Chemistry A, **117**(25), 5344-5353, 2013.

[82] O. G. Palanna, Engineering chemistry, Tata McGraw-Hill Education, 381, 2009.

[83] D. E. Sands, Introduction to crystallography, Courier Corporation, 1969.

[84] J. A. Ibers, W. C. Hamilton, International Tables for X-ray Crystallography: Revised and Supplementary Tables. Kynoch Press for the International Union of Crystallography, 1974.

[85] Q. Zhang, V. Bulone, H. Ågren, and Y. Tu, “A molecular dynamics study of the thermal response of crystalline cellulose Iβ”, Cellulose, **18**(2), 207-221, 2011.

[86] K. Kulasinski, S. Keten, S. V. Churakov, D. Derome, and J. Carmeliet, “A comparative molecular dynamics study of crystalline, paracrystalline and amorphous states of cellulose”, Cellulose, **21**(3), 1103-1116, 2014.

[87] C. M. Lee, J. D. Kubicki, B. Fan, L. Zhong, M. C. Jarvis, S. H. Kim, “Hydrogen-bonding network and OH stretch vibration of cellulose: comparison of computational modeling with polarized IR and SFG spectra”, The Journal of Physical Chemistry B, **119**(49), 15138-15149.

[88] T. Shen, P. Langan, S. Gnanakaran, A. D. French, and G. P. Johnson, “Shift in Conformational Flexibility of Soluble Cellulose Oligomers with Increasing Chain Length (No. LA-UR-08-07090; LA-UR-08-7090)”, Los Alamos National Laboratory (LANL), 2008.

[89] P. E. Mason, G. W. Neilson, J. E. Enderby, M. L. Saboungi, G. Cuello, and J. W. Brady, “Neutron diffraction and simulation studies of the exocyclic hydroxymethyl conformation of glucose”, The Journal of chemical physics, **125**(22), 224505, 2006.

[90] P. Chen, Y. Nishiyama, and K. Mazeau, “Torsional entropy at the origin of the reversible temperature-induced phase transition of cellulose”, Macromolecules, **45**(1), 362-368, 2011.

[91] K. H. Gardner, and J. Blackwell, “The structure of native cellulose”, Biopolymers, **13**(10), 1975-2001, 1974.

[92] F. Horii, A. Hirai and R. Kitamaru, “Solid-state 13 C-NMR study of conformations of oligosaccharides and cellulose”, Polymer Bulletin, **10**(7-8), 357-361, 1983.

[93] D. S. BIOVIA, Materials Studio, 8.0. San Diego, 2014.

[94] J. Zhang, Q. Zhang, T. T. Vo, D. A. Parrish, and J. N. M. Shreeve, “Energetic salts with π-stacking and hydrogen-bonding interactions lead the way to future energetic materials”, Journal of the American Chemical Society, **137**(4), 1697-1704, 2015.

[95] Y. Yoneda, K. Mereiter, C. Jaeger, L. Brecker, P. Kosma, T. Rosenau, and A. French, “van der Waals versus hydrogen-bonding forces in a crystalline analog of cellotetraose: cyclohexyl 4’-O-cyclohexyl β-d-cellobioside cyclohexane solvate”, Journal of the American Chemical Society, **130**(49), 16678-16690, 2008.

[96] P. Chen, Y. Nishiyama, J. L. Putaux, and K. Mazeau, “Diversity of potential hydrogen bonds in cellulose I revealed by molecular dynamics simulation”, Cellulose, **21**(2), 897-908, 2014.

[97] J. F. Matthews, C. E. Skopec, P. E. Mason, P. Zuccato, R. W. Torget, J. Sugiyama, M. E. Himmel, and J. W. Brady, "Computer simulation studies of microcrystalline cellulose Iβ", Carbohydrate Research, **341**(1), 138-152, 2006.

[98] D. A. Dikin, S. Stankovich, E. J. Zimney, R. D. Piner, G. H. Dommett, G. Evmenenko and R. S. "Preparation and characterization of graphene oxide paper", Nature, **448**(7152), 457-460, 2007.

[99] S. J. Eichhorn and G. R. Davies, "Modelling the crystalline deformation of native and regenerated cellulose" Cellulose, **13**(3), 291-307, 2006.

[100] F. Tanaka, T. Iwata, "Estimation of the elastic modulus of cellulose crystal by molecular mechanics simulation", Cellulose, **13**(5), 509–17, 2006.

[101] K. Tashiro and M. Kobayashi, "Theoretical evaluation of three-dimensional elastic constants of native and regenerated celluloses: role of hydrogen bonds", Polymer, **32**(8), 1516-1526, 1991.

[102] K. H. Meyer, Natural and synthetic high polymers, New York: Inter-Science Publishers, 1942.

[103] R. Meredith, "Mechanical properties of cellulose and cellulose derivatives", Recent advances in the chemistry of cellulose and starch, 213-239, 1959.

[104] W. J. Lyons, "Theoretical values of the dynamic stretch moduli of fiber-forming polymers", Journal of Applied Physics, **29**(10), 1429-1433, 1958.

[105] W. J. Lyons, "Theoretical value of the dynamic stretch modulus of cellulose", Journal of Applied Physics, **30**(5), 796-797, 1959.

[106] M. Bergenstrahle, L. A. Berglund, and K. Mazeau, "Thermal response in crystalline Iβ cellulose: a molecular dynamics study", The Journal of Physical Chemistry B, **111**(30), 9138-9145, 2007.

[107] I. Diddens, B. Murphy, M Krisch, and M. Müller, "Anisotropic elastic properties of cellulose measured using inelastic X-ray scattering", Macromolecules, **41**(24), 9755-9759, 2008.

[108] R. R. Lahiji, X. Xu, R. Reifenberger, A. Raman, A. Rudie, and R. J. Moon, Atomic force microscopy characterization of cellulose nanocrystals. Langmuir, **26**(6), 4480-4488, 2010.

[109] R. Wagner, R. J. Moon, J. Pratt, G. Shaw, and A. Raman, "Uncertainty quantification in nanomechanical measurements using the atomic force microscope", Nanotechnology, **22**(45), 455703, 2011.

[110] A. Pakzad, J. Simonsen, P. A. Heiden, and R. S. Yassar, "Size effects on the nanomechanical properties of cellulose I nanocrystals", Journal of Materials Research, **27**(3), 528-536, 2012.

[111] L. Liu, J. Zhang, J. Zhao, and F. Liu, "Mechanical properties of graphene oxides", Nanoscale, **4**(19), 5910-5916, 2012.

[112] C. Cao, M. Daly, C. V. Singh, Y. Sun, and T. Filleter, "High strength measurement of monolayer graphene oxide", Carbon, **81**, 497-504, 2015.

[113] C. Lee, X. Wei, J. W. Kysar, and J. Hone, "Measurement of the elastic properties and intrinsic strength of monolayer graphene", Science, **321**(5887), 385-388, 2008.

[114] B. Peng, M. Locascio, P. Zapol, S. Li, S. L. Mielke, G. C. Schatz, and H. D. Espinosa, “Measurements of near-ultimate strength for multiwalled carbon nanotubes and irradiation-induced crosslinking improvements”, Nature nanotechnology, **3**(10), 626, 2008.

[115] X. Zhang, S. Liu, H. Liu, J. Zhang and X. Yang, “Molecular dynamics simulation of the mechanical properties of multilayer graphene oxide nanosheets”, RSC Advances, **7**(87), 55005-55011, 2017.

[116] C. Gómez-Navarro, M. Burghard, and K. Kern, “Elastic properties of chemically derived single graphene sheets”, Nano letters, **8**(7), 2045-2049, 2008.

[117] J. W. Suk, R. D. Piner, J. An, and R. S. Ruoff, “Mechanical properties of monolayer graphene oxide”, ACS nano, **4**(11), 6557-6564, 2010.

[118] A. R. Khoei, M. S. Khorrami, “Mechanical properties of graphene oxide: A molecular dynamics study”, Fullerenes, Nanotubes and Carbon Nanostructures, **24**(9), 594-603, 2016.

[119] R. A. Soler-Crespo, W. Gao, P. Xiao, X. Wei, J. T. Paci, G. Henkelman, and H. D. Espinosa, “Engineering the mechanical properties of monolayer graphene oxide at the atomic level”, The Journal of Physical Chemistry Letters, **7**(14), 2702-2707, 2016.